

CHAPTER 6

INTERNAL WAVE FIELDS ANALYZED BY IMAGING VELOCIMETRY

John Grue

*Mechanics Division, Department of Mathematics, University of Oslo
P.O. Box 1053 Blindern, 0316 Oslo, Norway
E-mail: johng@math.uio.no*

We review recent laboratory measurements of internal waves using Particle Tracking Velocimetry and Particle Image Velocimetry. The methods enable accurate recordings of the wave induced velocity and vorticity fields. Global properties like wave length and wave speed are obtained from the measurements. Solitary waves and dispersive wave trains in two-layer fluids with an upper layer that is either homogeneous or linearly stratified, and a lower layer that is homogeneous, are investigated. The measurements provide references for mathematical models and are used to judge their applicability. Particular focus is paid to solitary waves that exhibit convective breaking, shear instability, how wave breaking changes the global wave properties, how solitary waves break at a submerged ridge or shelf, and how the wave breaking induces transport of suspended particles. Run-up of very long internal waves at a shelf-slope is found to introduce strong fluid velocities where the pycnocline meets the slope. The experiments are used to interpret observations in large scale.

1. Introduction

A physical laboratory simulator represents a tool for investigating complex flow phenomena where theoretical models have shortcomings or do not exist. Laboratory experiments of internal waves (and other flows) may be used to explain observations in the sea and may serve as guidance in developing theories of internal wave propagation where a breaking of the flow eventually is inherent. The experimental wave tank may be used to study waves with very large amplitudes, waves that propagate along thin or broad pycnoclines, conditions that lead to breaking of the waves, properties of internal waves that break and internal waves that interact with a sub-sea ridge or shelf-slope. Laboratory experiments represent an important complement to

theoretical and numerical modelling of internal waves. Measurements may be used to confirm mathematical solutions and are useful to judge the range of validity and possible limitations of simulation models.

Our main interest in studying internal waves was motivated by requests from industry, including the magnitude of the fluid velocities induced by internal waves, the vertical motion of pycnoclines in the deep ocean, and interpretation of sudden temperature or current spikes observed in the ocean close to the sea floor. Internal wave loading on pipelines, or on a submerged floating tunnel that was proposed as connection across a Norwegian fjord, represented other questions from industry. Marine biologists observed large vertical periodic motion of fish and navigation of fish along density contours in the ocean, and questioned if this could be explained by internal wave motion. Further, understanding and description of currents and waves in fjords, including the motion of interfaces in the sea, are important for a proper management of the ecosystem. The questions supported our general curiosity on the phenomenon of internal waves, the experimental measurements and the mathematical modelling of the waves.

Descriptions of internal waves in large scale may be found in, e.g., Osborne, Burch and Scarlet¹, Ostrovsky and Stepanyants², Huthnance³. Both internal solitary waves of large amplitude (Pingree and Mardell⁴, Apel et al.⁵, Stanton and Ostrovsky⁶) and dispersive wave trains (Gjevik and Høst⁷) are observed. Mathematical description of the waves in terms of weakly nonlinear Korteweg-de Vries (KdV) and Benjamin-Ono equations may be employed for small and moderate wave amplitudes. Fully nonlinear theories are in general required for a proper modelling when the excursion of the isopycnals become comparable to their average depth (Holyer⁸, Meiron and Saffman⁹, Amick and Turner¹⁰, Turner and Vanden-Broeck^{11,12}, Evans and Ford¹³, Grue et al.^{14,15,16}, Lamb¹⁷).

While several papers describe the mathematical modelling of the waves (solitary waves, periodic or unsteady wave trains), comparatively few experimental papers on the subject are published. The most important experimental investigations on nonlinear internal waves are summarized here. The amplitude-wave length relationship of interfacial solitary waves with small to moderate amplitude was experimentally determined by Koop and Butler¹⁸, Segur and Hammack¹⁹, Kao, Pan and Renouard²⁰. Comparisons with weakly nonlinear theories were made. In the latter work the fluid velocity was measured using hot-film probes. Michallet and Barthélemy²¹ measured profiles and speeds of solitary waves in a two-fluid system, with the amplitude ranging from small to relatively large values. Their attempts to investigate wave amplitudes close to the maximal one were prevented by

breaking during the wave generation process.

Internal solitary waves of mode two propagating along the pycnocline were experimentally investigated by Davis and Acrivos²², Maxworthy²³ and Stamp and Jacka²⁴. The small scale experiments in the latter work exhibited wave amplitudes that were up to five times the half-width of the pycnocline. Internal waves interacting with a shelf-slope show formation of turbulent boluses travelling up a slope, intense breaking where the pycnocline intersects the slope and partial reflection of the incoming waves (Cacchione and Southard²⁵, Wallace and Wilkinson²⁶, Kao et al.²⁰, Helfrich²⁷). Small particles may be transported along the pycnocline in the direction away from the slope as a consequence of the breaking (Michallet and Ivey²⁸). Internal waves interacting with a submerged ridge have been experimentally studied by Wessels and Hutter²⁹, Vlasenko and Hutter³⁰, Svein et al.³¹, Guo et al.³².

Up to now, measurements of internal waves were usually carried out using resistance wave gauges, ultrasonic probes or hot-film probes. We shall in this paper review recent measurements using the optical methods Particle Tracking Velocimetry (PTV) and Particle Image Velocimetry (PIV). Efficient processing of the relatively large data sets are enabled by powerful computers. It is indeed the computer efficiency and rapid storage techniques gained during the last decade that have made PTV and PIV tractable. Velocity profiles, local vorticity and global properties like propagation speed and wave length are derived from the velocimetry. Details of breaking processes are quantified by the methods. Comparisons with mathematical and numerical computations are performed whenever possible.

The paper is organized as follows: The experimental wave tank and the PTV and PIV methods in use are summarized in section 2. An estimate of how close the particles follow the fluid flow is given. Wave propagation along a thin pycnocline is discussed in section 3. Measurements of solitary waves of depression with amplitudes ranging from a small value up to the maximal theoretical wave amplitude are discussed. Experiments with dispersive wave trains are included. Breaking and broadening of solitary waves propagating in a two-fluid system with a linear stratification and a homogeneous fluid in the upper and lower layer, respectively, are discussed in section 4. Features of waves breaking at a submerged ridge are reported in section 5. The motion of internal waves, the induced breaking and the run-up at steep or mild-sloping beaches are discussed in section 6. Vertically induced velocities in the ocean identified by fish motion are described in section 7. Section 8 contains a description of the fully nonlinear mathematical/numerical reference models, while section 9 is a conclusion.

2. The experimental wave tank

2.1. *The wave tank and stratification*

We shall mainly report experiments that were carried out in the Hydrodynamic Laboratory at the University of Oslo. Sections of a wave tank 0.5 m wide, 1 m deep and 6.2, 12.3 or 21.4 m long were used. Each experiment began by calibrating a two-fluid system where a lower layer of brine had density $\rho_1 = 1.022\dots\text{g/cm}^3$ and depth h_1 . The top layer was either of fresh (homogeneous) water or had a linear stratification with density $\rho_2=0.999\dots\text{g/cm}^3$ at the upper surface of the layer. The depth of the upper layer was h_2 . The density profiles were recorded by a Yokogawa SC12 meter which determines the density from the local conductivity of the fluid. Reference measurements were taken at some selected locations using a Mettler-Toledo DA-300M density meter which determines the density to four decimal places. Some of the runs (described in sections 3.2, 6.2) were performed in a smaller wave tank with dimensions 0.3 m \times 0.7 m \times 7 m (width, depth, length).

2.2. *Particle tracking and particle image velocimetry*

For the benefit of the reader we briefly summarize the most important points of the PTV and PIV methods used in the experiments (Grue et al.^{14,15}, Svein et al.³¹). The PTV method traces individual particles in sequences of images. The method is ideal when the local fluid acceleration is small which is true for the slowly progressing internal waves in focus.

Vertical sections of the wave tank were illuminated for subsequent recording of the wave motion. The light sheets were parallel to the side of the tank, 5 cm thick and had a distance of 10 cm from the glass wall. Crunched particles of pliolite VTAC with diameter in the range 0.8–1 mm were in the viewing sections seeded to the fluid. The density of the pliolite is approximately 1.0228 g/cm³. Particles were treated using a wetting agent to obtain an effectively neutral buoyancy in the entire range of the density profile. The viewing sections were typically 50 cm \times 40 cm large. Monochrome COHU 4912 CCD cameras with a resolution 575 \times 560 of pixels were used in the flow recordings. A particle at rest was normally covered by four pixels in the CCD-chip. The effective shutter speed (using a mechanical shutter) was usually 1/100 s. (In some initial experiments the shutter speed was 3/100 s.) The time between each frame is 1/25 s.

The video recordings were digitized by a frame grabber card for subsequent analysis. In the experiments presented here we typically identified 800-4000 particles in each frame. Particles were traced during five frames us-

ing the DigImage program developed and described by Dalziel³³. A perspex plate with reference coordinates was submerged in the fluid and recorded after each set of runs. Reference points were mounted to the wave tank. The mapping coordinates between the recording section and the camera is linear.

In some of the waves the acceleration was not always small. This is true when breaking of the flow was observed. We could not trace particles long enough for the PTV algorithm to be effective, for example. Data processing using PIV was then used to estimate the velocity field. For the PIV algorithm we implemented the method outlined by Willert and Gharib³⁴ using an interrogation window shifting procedure of Westerweel, Dabiri and Gharib³⁵. The images were interrogated in three steps where the two first steps were used to estimate the window shift with integer accuracy. In the final step the displacement was estimated to sub-pixel accuracy using a three point Gaussian peak fit. Images were interrogated using windows of 32×32 pixels. In some experiments 64×64 pixels were used due to insufficient particle seeding. A signal to noise ratio filter was used to validate the final velocity vectors. A local median filter effectively removed vectors deviating significantly from their neighbours. The implementation is documented in full in Sveen³⁶.

2.3. Relative accuracy of the optical method

The difference $\Delta \mathbf{V}$ between the fluid velocity and the velocity of a seeded particle may be analysed using the equation of momentum for the particle, assuming that the Stokes drag is much less than the time derivative of the particle momentum, i.e. $|m\dot{\mathbf{V}}| \gg |6\pi\rho\nu R\Delta \mathbf{V}|$. Here a dot denotes time derivative, ν the kinematic viscosity and R , \mathbf{V} , $m = (4\pi/3)\rho R^3$ the radius, velocity and mass of the particle (assuming neutral buoyancy), respectively. ρ denotes fluid density. This gives $|\Delta \mathbf{V}| \ll \alpha|\dot{\mathbf{V}}|$ where $\alpha = m/6\pi\rho\nu R = 2R^2/9\nu$. The acceleration is estimated by $|\dot{\mathbf{V}}| \sim |\mathbf{V}_m|/T$ where $|\mathbf{V}_m|$ denotes a typical maximal velocity and T a typical period of the flow. Characteristic values of $|\mathbf{V}_m|$ and T in the present experiments are 10 cm/s and 5–10 s, respectively. With $R = 0.5$ mm and $\nu = 10^{-6}$ m²/s we find

$$\frac{|\Delta \mathbf{V}|}{|\mathbf{V}_m|} \ll \frac{2R^2}{9\nu T} \sim 0.005 - 0.01. \quad (1)$$

The corresponding particle Reynolds number $Re = 2R|\Delta \mathbf{V}|/\nu$ is less than unity. The seeded particles thus quite closely follow the fluid motion, with an accuracy indicated by (1).

The accuracy of the digital tracing of a particle may be estimated as follows: We assume that the position and displacement of each particle is determined with an accuracy better than the length of a pixel which corresponds to about 1 mm in physical space in our case. (Dalziel³³ found in his experiments that the position of a particle was determined with an accuracy of about 0.2 times the pixel length.) A particle with a typical velocity of 10 cm/s, traced during a sequence of five frames, i.e. a time interval of 0.2 s, moves a distance of 2 cm. This means that the relative error in the particle displacement and the velocity is at most $1\text{mm}/2\text{cm}=5\%$. This is a much larger figure than the error in (1). We have found that a relative error of the measured velocities is approximately in agreement with the error analysis just described. We find, for example, that the measured fluid velocity induced by a solitary wave, relative to the linear long wave speed c_0 of the two-layer fluid, has a deviation of about 7–8% at most, from a line fitted to all experiments that were made, see Fig. 2c. Our results include analysis using both PTV and PIV, preferring the method giving the best accuracy for the actual run. We note that in all practical applications it is possible to obtain the same accuracy using PTV and PIV.

3. Motion along a thin pycnocline

3.1. *Solitary waves*

Investigations of large amplitude solitary waves propagating in a two-layer fluid represented a main focus of the laboratory studies that were undertaken. The waves were measured in the wave tank (dimensions are previously given) using the procedure described above: A two-layer fluid with a lower layer of brine and an upper layer of homogeneous fresh water was calibrated. In most of the runs the lower layer depth was $h_1 = 62$ cm and the upper layer depth $h_2 = 15$ cm which means a depth ratio of $h_1/h_2 = 4.13$. The thickness of the pycnocline was 1–2 cm.

Vertical sections of the wave tank were illuminated for subsequent recording of the wave motion. Solitary waves were produced by trapping a volume of light fluid behind a gate that was lowered in one end of the wave tank. Upon removal of the gate the initial depression rather quickly was transformed into a solitary wave propagating along the tank. A single solitary wave was in each experiment produced by a combined adjustment of the position of the gate and the added volume (see Fig. 1a). The wave amplitude ranged from a rather small value to about the maximal possible one, as indicated by the measurements presented in Fig. 2c. The video cameras placed along the tank, at positions 4.5 m and 10.4 m from the end

of the tank where the waves were generated, recorded the wave induced motion of the particles that was seeded into the fluid.

From the recordings we determined the induced velocity profiles, speed and shape of the waves. The velocity measurements of the individual runs were scaled by the linear long wave speed of the two-fluid system given theoretically by

$$c_0^2 = \frac{gh_1h_2(\rho_1 - \rho_2)}{\rho_2h_1 + \rho_1h_2}, \quad (2)$$

where g denotes the acceleration of gravity. The effect on the wave and fluid velocities due to small variations of the relative density jump in the different runs was then ruled out.

The wave speed c was estimated by the elapsed time of the wave propagation between the two viewing sections (at 4.5 and 10.4 m, including accurate reference points) divided by distance. The confined pycnocline is very visible due to a higher concentration of particles there than elsewhere. The pycnocline motion was determined by visual inspection of video images. The wave speed scaled by the theoretical linear wave speed determined from eq. (2) is visualized in Fig. 2a. The wave speed is seen to grow at a rate that is decreasing with amplitude. At maximal amplitude the growth is zero. The experimental wave amplitudes are found to undergo a small reduction during the propagation due to the effect of viscosity. The decrease of the amplitude between the recording stations is indicated by the horizontal bars in the figure. (The largest amplitude refers to the first recording station.)

Wave profiles were obtained from the video images by first tracing the vertical motion of the middle position of the pycnocline, as function of time. The recorded motion was then plotted versus time multiplied by the computed (and measured) wave speed c . Supplementary estimates of the pycnocline motion were obtained by tracing the jump in the velocity profile (across the pycnocline). The two methods give the same result, see Fig. 1b.

The main output from the velocimetry is the velocity field induced by the wave motion. The velocities in any position of the wave were determined. An example of the velocity profile at the wave crest is visualized in Fig. 2b. Results from a total of 10 different runs with slightly different pycnocline thicknesses are included. The consistent results illustrate the robustness and accuracy of the experiments. We were also interested in measuring the induced fluid velocities in the layers as function of wave amplitude. Results for the horizontal fluid velocity in the upper layer are obtained for the whole range of possible wave amplitudes (Fig. 2c). The maximal theoretical

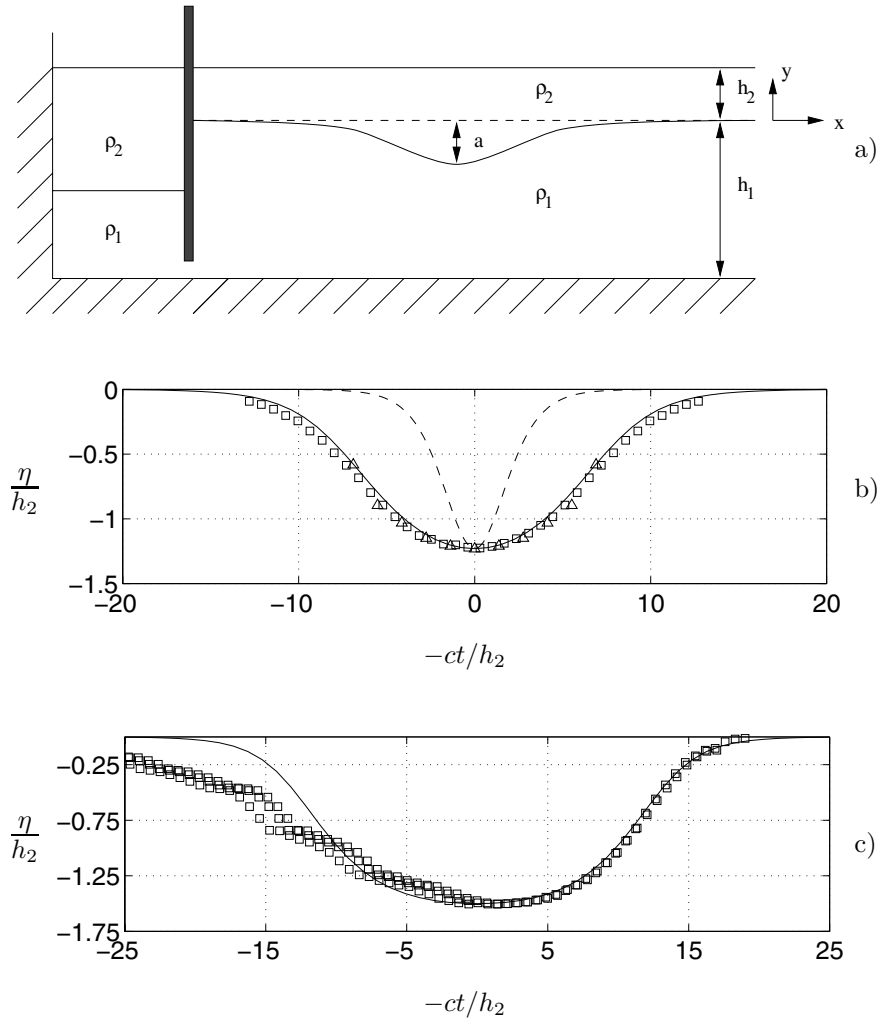


Fig. 1. Solitary waves propagating along a thin pycnocline. Sketch of experiment (upper). Profiles $\eta(ct)$ of waves with amplitude $a/h_2 = 1.23$ (mid) and $a/h_2 = 1.51$ (lower). Squares: measured pycnocline. Triangles: measured jump in velocity. Solid line: fully nonlinear theory. Dashed line: KdV theory. $h_1/h_2 = 4.13$. From Grue et al.¹⁵. Reproduced with permission by J. Fluid Mech.

amplitude in these experiments is $a/h_2 = 1.55$ (accounting accurately for the slightly small difference between the densities ρ_1 and ρ_2). The corresponding theoretical maximal fluid velocity is $u/c_0 = 0.77$. In the figure the function $(u/c_0)/(a/h_2)$ is plotted. For very small a/h_2 the function is close

to unity. At maximal amplitude the value of $(u/c_0)/(a/h_2)$ is about 0.5 for the actual depth ratio between the layers.

The experimental solitary waves may be computed employing a theoretical two-layer model where in the latter the thin pycnocline is replaced by an interface separating the motion in the upper and lower layer. An interesting aspect of the campaign is that the fully nonlinear model may be used to check the PTV method. The high precision computations provide a theoretical reference when the experimental conditions fit with the assumptions of the theory. Vice-versa, a fit between theory and experiment documents the applicability of the theoretical interface model.

Fully nonlinear computations of solitary waves were performed using the theoretical-numerical two-layer interface model developed by Grue et al.^{14,15}. The results exhibit a surprisingly good agreement between measurements and theory for the whole range of wave amplitudes. The agreement is good even for a pycnocline which is not very sharp. The range up to the highest waves is covered. We were particularly interested in investigating experimental solitary waves with amplitudes as close as possible to theoretical maximum, which in the Boussinesq limit ($\Delta\rho/\rho \ll 1$) means that the pycnocline moves to a position that is mid-way in the fluid. (This implies the simple formula $a_{max}/h_2 = \frac{1}{2}(h_1/h_2 - 1)$ for the maximal wave amplitude, with numerical value 1.56 when $h_1/h_2 = 4.13$.)

We observe a good correspondence between theory and experiment for the profile of the maximal wave, in the leading part of the wave (Fig. 1c). In this experiment the minimal value of the Richardson number, estimated from velocimetry, was 0.07. Local breaking of the flow due to a shear instability was then expected. Indeed, breaking is observed in the tail of the wave. The shear instability is very visible. Instability and subsequent breaking of the flow cannot be predicted by the theoretical two-layer model.

The results in Fig. 2c indicate a relative accuracy of the measurements of about 7-8%. This represents the maximal deviation of u/c_0 from the theoretical line and from a fitted line of the recordings.

We have here studied the motion of solitary depression waves. The polarity of the solitary waves is determined according to the sign of the coefficient $h_2^2\rho_1 - h_1^2\rho_2$. The waves are depression or elevation waves when this factor is negative or positive, respectively.

Korteweg-de Vries theory provides a supplementary reference when the wave amplitude is small. The assumption of a weak nonlinearity is violated for moderate and large wave amplitudes, however. The amplitude range where KdV theory is valid is found to be rather small (a/h_2 less than about 0.4).

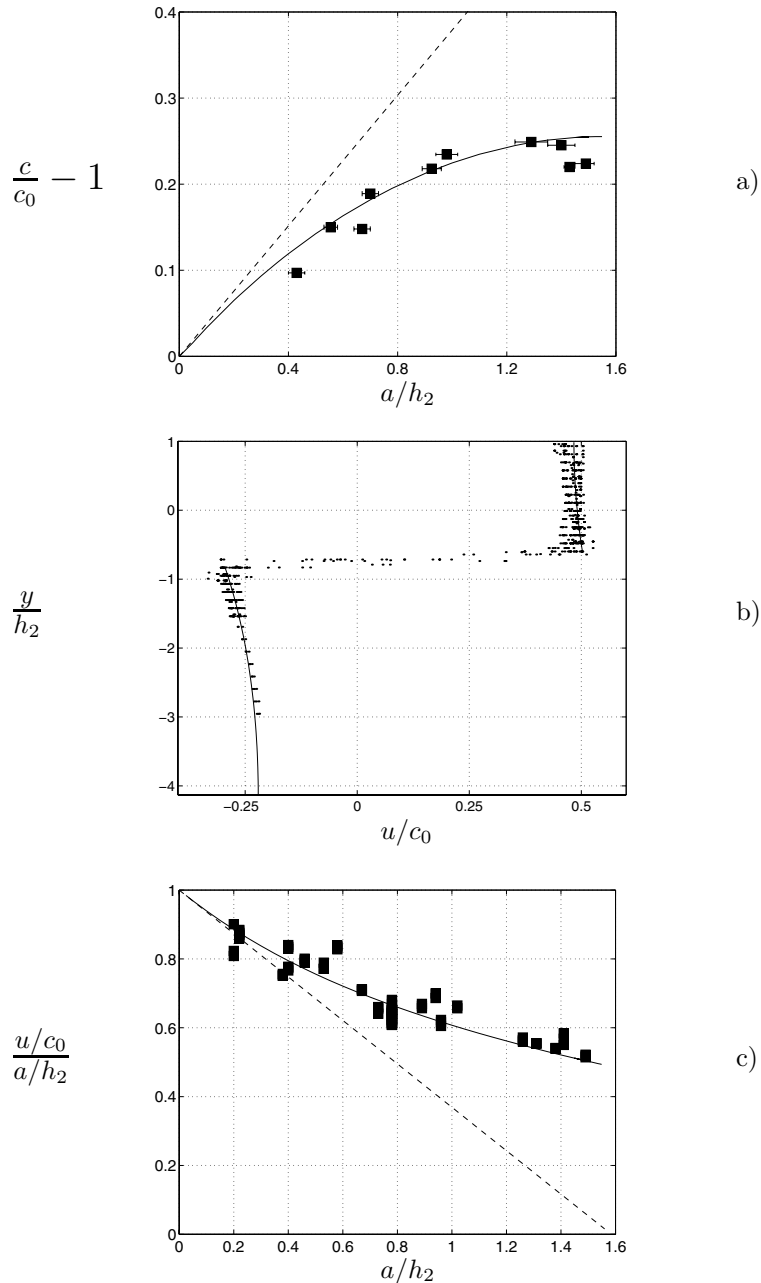


Fig. 2. Solitary waves. a) Excess speed vs. wave amplitude, b) velocity profile above and below crest ($a/h_2 = 0.78$), c) nondimensional velocity in upper layer (at level $y = -h_2/2$) vs. nondimensional amplitude a/h_2 . $h_1/h_2 = 4.13$. From Grue et al.¹⁵. Reproduced with permission by J. Fluid Mech.

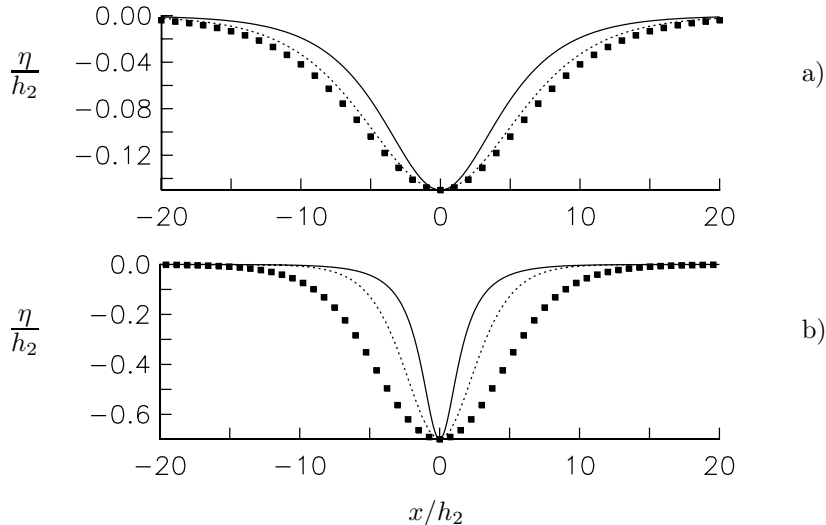


Fig. 3. Fully nonlinear wave profile (square), KdV (dots) and Intermediate-long-wave equations (solid line). a) $a/h_2 = 0.15$, b) $a/h_2 = 0.7$. $h_1/h_2 = 4$, $\rho_2/\rho_1 = 0.9$. From Grue et al.¹⁴. Reproduced with permission by J. Fluid Mech.

It may be questioned if the Intermediate-long-wave-equations¹⁹ may be more relevant than KdV theory in the present examples, where the wave length $L/h_2 \sim 10-20$ is not much longer than the depth ratio $h_1/h_2 = 4.13$. The Intermediate-long-wave-equations have very limited range of validity and represent a poorer approximation than KdV theory, however (Fig. 3). This is true even if the wave length is comparable to the total depth of the fluid. Extensions based on the KdV and the BO equations, valid for solitary waves with large amplitude, are discussed by Ostrovsky and Grue³⁷.

3.2. Dispersive wave trains

Experiments were also performed with a portion of brine trapped by the gate. This corresponds to an initial condition where a part of the interface has an elevation. The resulting wave system is a dispersive wave train propagating along the tank with the longer waves travelling faster than the shorter ones. The mechanical energy per wave length is relatively much smaller than the wave energy transported by a single solitary wave. The induced fluid velocities are correspondingly smaller (Fig. 4). The experimental waves are adequately modelled by the (linear) Cauchy-Poisson problem modified to interfacial flows (Carlin³⁸, Hald³⁹). The experiments and theory

document wave systems that may be generated upon release of a volume of heavy water into a two-layer system. Such wave trains are observed in large scale in Skagerak off the southern coast of Norway. During summer a thermocline is developed in the sea with an average depth of 15 m, a relative jump in density of 3.7×10^{-3} , with corresponding linear long wave speed $c_0 \simeq 70$ cm/s. Wave groups show leading waves that typically are 1.5 km long, see Gjevik and Høst⁷. The wavenumber at any position of the wave train is implicitly determined by: $d/dk[(x/t)k - \omega(k)] = 0$, where $\omega^2 = g'k/(\coth kh_1 + \coth kh_2)$, k the wavenumber, x horizontal position, t time, ω wave frequency, $g' = g\Delta\rho/\rho$, g acceleration of gravity, $\Delta\rho/\rho$ relative jump in density. The laboratory results and the mathematical model predictions give an indication of the magnitude of the fluid velocities that are induced by the waves in large scale. (Nondimensional velocity in the upper layer, $u/c_0 \sim 0.1$ corresponds to nondimensional interfacial vertical excursion, $a/h_2 \sim 0.15$.)

4. Solitary waves that break

Heating from sun may result in a linear stratification of the upper part of the ocean. Such a stratification is season-dependent and is observed at many locations. The thickness of the linearly stratified layer typically ranges from some tens of meters to a few hundreds. Examples are represented by the Sulu Sea (Fig. 5) and the Knight Inlet in British Columbia (Farmer and Smith⁴⁰). Another example is off the northern coast of Norway, see section 7. Internal wave propagation along such a stratification may be studied in the laboratory wave tank by preparing a fluid where an upper part of the undisturbed water column has a constant Brunt-Väisälä frequency and a lower part is homogeneous.

The properties of internal solitary waves propagating along such a stratification were investigated experimentally and theoretically by Grue et al.¹⁶. The waves were generated using the same procedure as for the two-layer fluid with constant density in the layers (sections 2, 3). In all experiments reported here the thickness h_1 of the lower homogeneous fluid is 4.13 times the thickness h_2 of the upper fluid, where the latter has a linear stratification (and the density is continuous in the transition between the layers). The recorded velocities in the experiments were scaled by the linear long wave speed of the two-fluid system determined by¹⁶

$$\frac{N_0 h_2}{c_0} \cot \frac{N_0 h_2}{c_0} + \frac{h_2}{h_1} = 0, \quad (3)$$

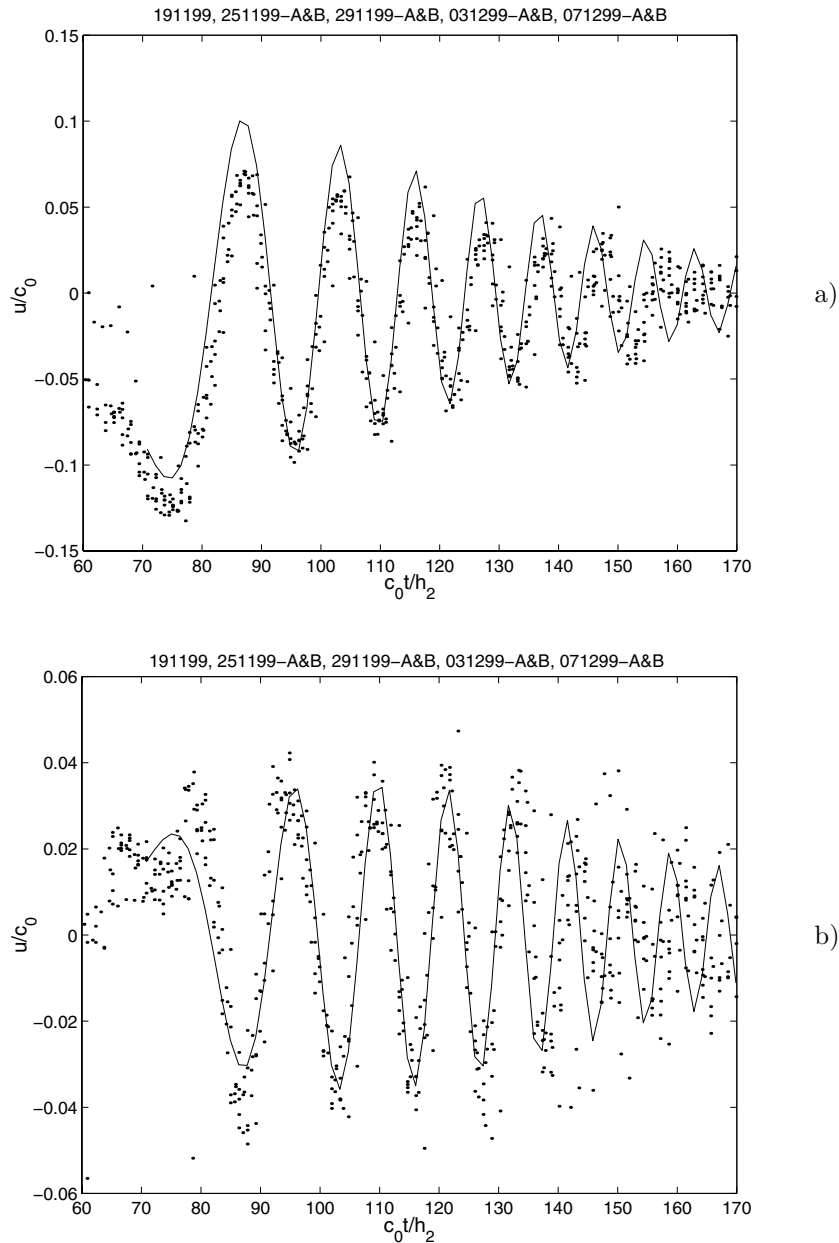


Fig. 4. a) Horizontal velocity in upper layer and b) below pycnocline. Dispersive waves. PTV measurements (dots), linear theory - solution of the Cauchy-Poisson problem for two-layer interfacial flows (solid line). Recording position 6.95 m from end of wave tank. Elevation of pycnocline behind gate: 5 cm. $h_1 = 10$ cm, $h_2 = 60$ cm. Position of gate at 0.42 m. Adapted from Hald³⁹.

where $N_0^2 = (\Delta\rho g)/(\rho_0 h_2)$ denotes the Brunt-Väisälä frequency at rest and c_0 is obtained for $N_0 h_2/c_0$ in the interval $(\pi/2, \pi)$. The linear long wave speed becomes $c_0 = N_0 h_2/1.711..$ in the experiments discussed, where the ratio h_1/h_2 equals 4.13.

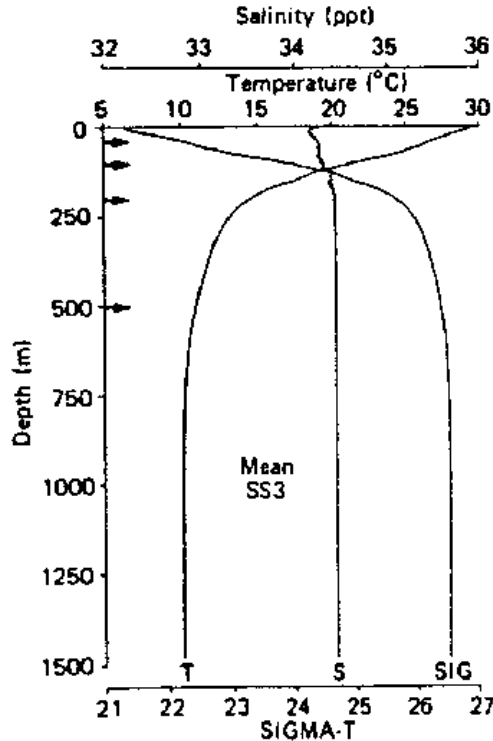


Fig. 5. Linear stratification in the Sulu Sea (Apel et al.⁵, Fig. 3), reprinted from J. Phys. Oceanogr., 15.

First we study the solitary wave speed c . This is taken as the (horizontal) speed of a vertical line through the approximate centre of the wave, characterized by a vanishing vertical fluid velocity, and is estimated by the median of the vectors that are available in the velocity maps. The measurements of c exhibit an almost linear increase with wave amplitude. (For $a/h_2 \ll 1$ the fully nonlinear, fully dispersive computations give $c/c_0 - 1 \simeq 0.584 a/h_2$, while KdV theory gives $c/c_0 - 1 \simeq 0.605 a/h_2$.) The correspondence between experiment and theory is good (Fig. 6). The wave speed plot does

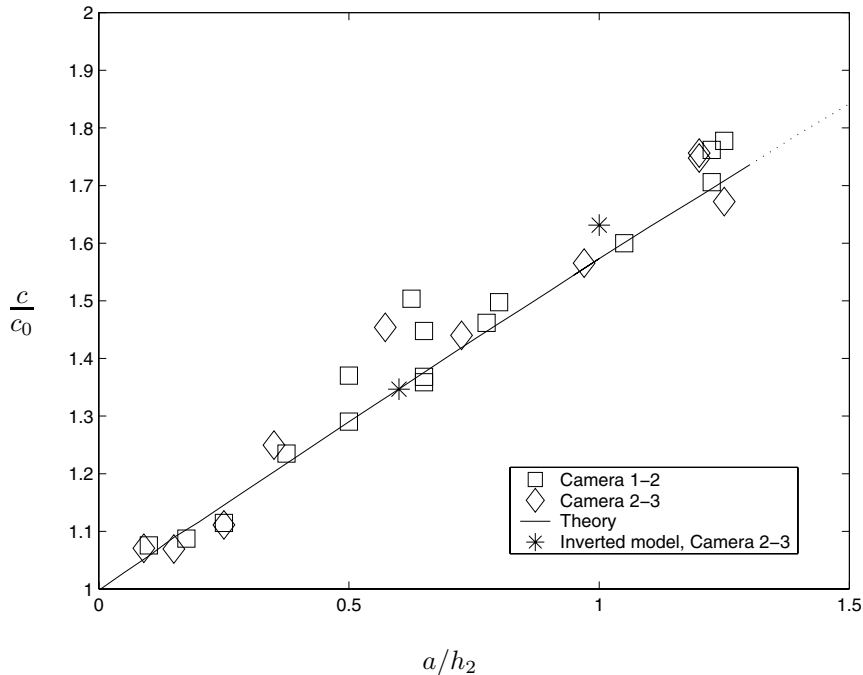


Fig. 6. Propagation speed c vs. wave amplitude. Symbols: measurements. Solid line: theory. From Grue et al.¹⁶. Reproduced with permission by J. Fluid Mech.

not indicate that a saturation of the wave, in the form of a maximal value of the amplitude, exists. This is unlike what was observed for a two-layer fluid with constant density in each layer. Another important difference from the previous two-layer fluid is that an abrupt velocity transition across the thin pycnocline is replaced by a smooth velocity field. The maximal fluid velocity is now occurring at the top of the water column and is significantly larger than with the other two-fluid system, for otherwise same wave amplitude. The variation of the horizontal velocity profile during the passage of a solitary wave is visualized in Fig. 7. The induced fluid velocity in the upper part of the upper layer is rather pronounced despite the relatively modest nondimensional wave amplitude of $a/h_2 = 0.4$. There is again a good correspondence between experiment and theory.

The wave motion introduces a nonzero vorticity field in the stratified fluid. Vorticity profiles are obtained from the particle imaging measurements using a finite difference operator, i.e., $df/dx_i = (2f_{i+2} + f_{i+1} -$

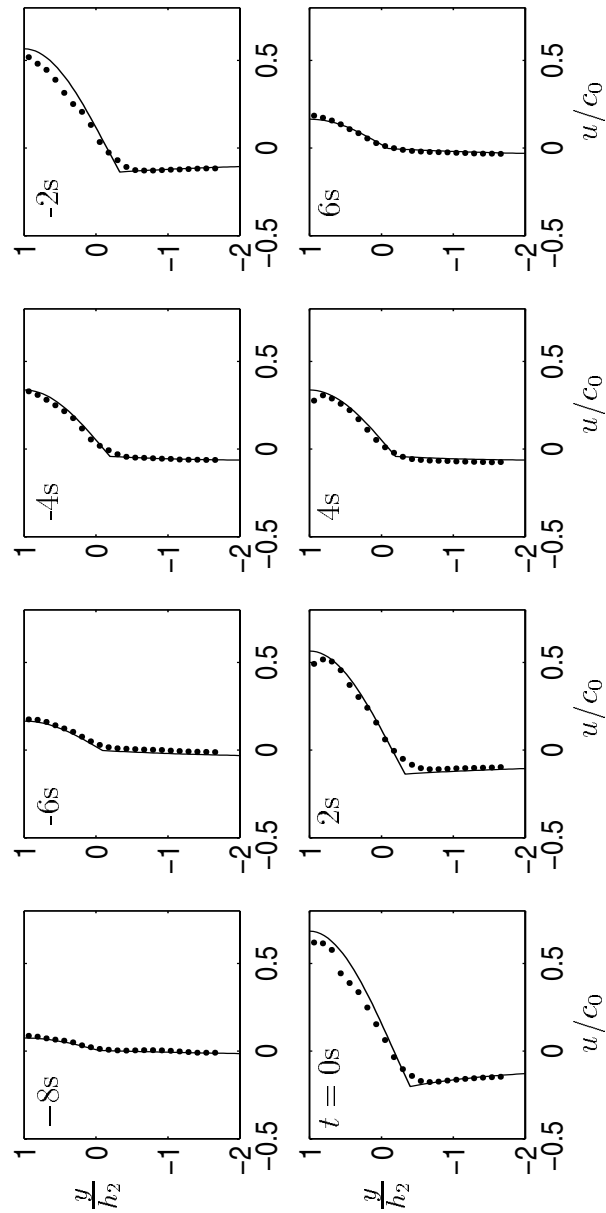


Fig. 7. Time series of passage of wave. Horizontal velocity u/c_0 as function vertical coordinate. Symbols: measurements. Solid line: theory. From Grue et al.¹⁶. Reproduced with permission by J. Fluid Mech.

$f_{i-1} - 2f_{i-2})/(10\Delta X)$. The experimental vorticity estimates are supported by the fully nonlinear computations for nonbreaking waves (Fig. 8a). Breaking of the waves is manifested by pronounced spikes in the vorticity field. A pronounced negative vorticity is observed at a level of $y/h_2 = -0.3$ in Fig. 8b, for example. The spike corresponds to a vortex seen in the velocity field and is caused by convective breaking. The maximal value of the vorticity in the series of experiments reported here is $|\omega|/(c_0/h_2) \simeq 3$, a result that is true for the largest waves. With $N_0 h_2/c_0 = 1.711\dots$, the maximal value of the vorticity relative to the Brunt-Väisälä frequency becomes, about, $\omega/N_0 \simeq 1.7$.

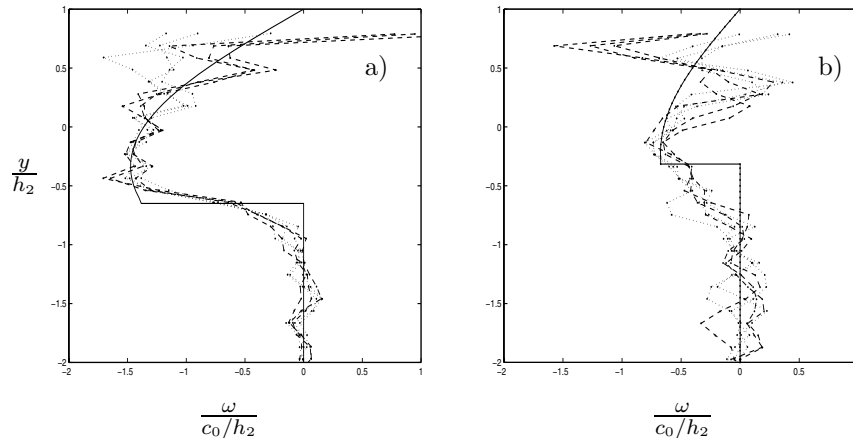


Fig. 8. Vorticity (ω) at crest of wave vs. vertical coordinate. a) Without breaking. b) with breaking. Solid line (theory, $a/h_2 = 0.65$), other lines (experiments). From Grue et al.¹⁶. Reproduced with permission by J. Fluid Mech.

For increasingly larger solitary waves, both the wave speed c and the induced fluid velocity relative to c grow until a saturation is reached. The limiting mechanism of the waves is found to be convecting breaking taking place when the induced fluid velocity attempts to exceed the wave speed. The convective breaking is observed in a region in the centre of the wave in the upper fluid. In the breaking region the fluid velocity has the form $\mathbf{v} = c\mathbf{i} + \mathbf{v}'$, where $c\mathbf{i}$ denotes the wave velocity and \mathbf{v}' a velocity field where $|\mathbf{v}'| \ll c$. (The waves transport a body of mass.) The vector \mathbf{i} denotes the horizontal unity vector along the direction of the wave propagation. The horizontal velocity profile above wave crest is characterized by u/c being

unity in a vertical range corresponding to almost the thickness of the upper layer (Fig. 9a–b).

The experimental waves exhibit broadening when breaking occurs (Fig. 9c). The nondimensional wave amplitude then exceeds about 0.8–0.9. (The theory predicts $u/c = 1$ for $a/h_2 = 0.855$.) The broadening effect found here is entirely different from the mechanism taking place in a two-fluid system with constant density in the layers. Then the limiting amplitude and limiting wave speed, and thereby the broadening of the waves, are determined by a finite total depth of the fluid (Amick and Turner¹⁰, Turner and Vanden-Broeck¹²), a result which is experimentally confirmed by the results in section 3.

We note that in the present two-layer fluid a solitary wave (of mode one) always exhibits an excursion out of the layer with linear stratification. Observations in the wave tank, and computations, confirm this result (results not shown). The polarity of the solitary waves may be determined analytically from the sign of the coefficient of the quadratic nonlinear term in weakly nonlinear KdV- or Intermediate-long-wave theory. This shows that the polarity is always the same for a two-layer fluid where one layer is linearly stratified and the other layer is homogeneous (and the stratification is continuous), see also Grue et al.¹⁶ eq. (8.1).

The results exhibit good correspondence between experiment and theory up to breaking. The fully nonlinear inviscid theory does neither explain the breaking nor the broadening of the waves observed in the experiments, however.

5. Wave-breaking at a submerged ridge

A solitary wave that interacts with a submerged ridge undergoes a local distortion that causes a scattering of the wave. Mechanical energy may be lost if breaking occurs. The case of a solitary wave incident normal to a long-crested ridge was experimentally investigated using PTV and PIV by Sveen et al.³¹. A stably stratified two-fluid system had homogeneous fluids in each layer. Conditions leading to breaking at the ridge and transmission of the solitary waves represented the main objectives.

We summarize the features that is characteristic for strong interaction between wave and ridge. The incoming internal solitary waves break during the deformation if the amplitude relative to the local depth at the top of the ridge exceeds a certain level. The breaking process is illustrated in Fig. 10. The incoming wave is in this case interacting with a relatively wide ridge. More specifically, the parameters in the experiment were: lower layer

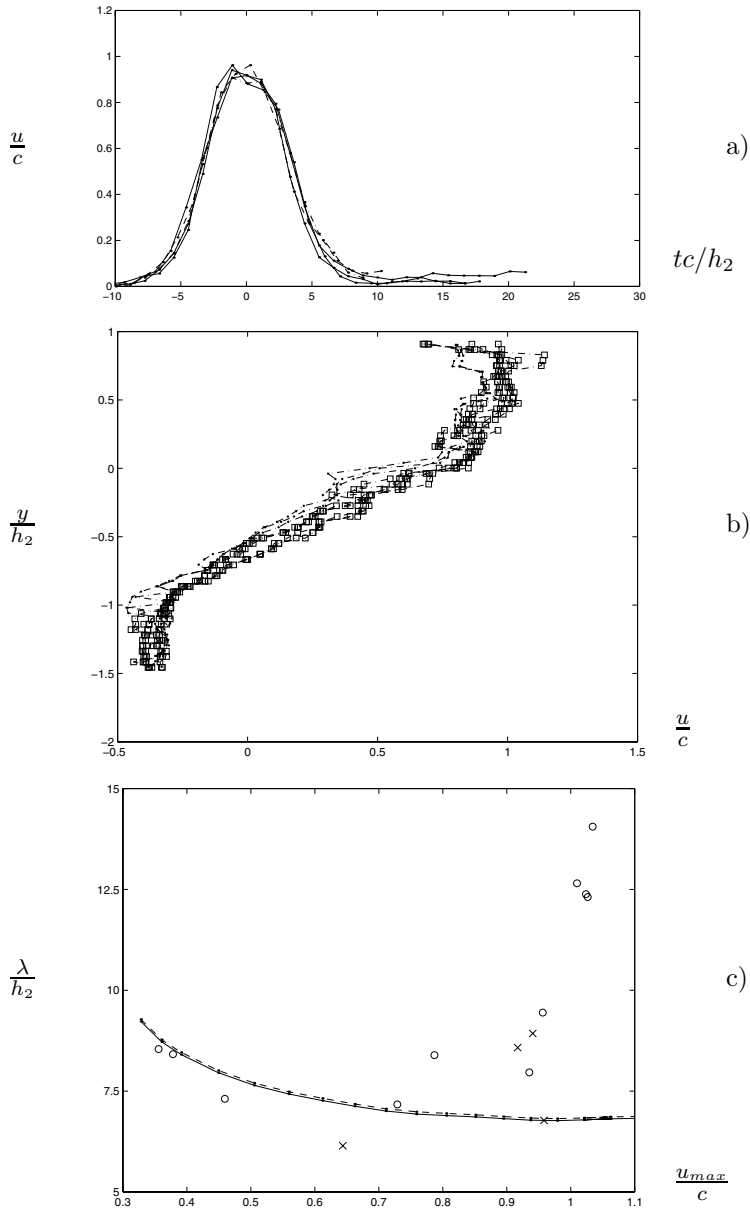


Fig. 9. a) Wave induced horizontal velocity at the free surface as function of time (initial volume 100 dm^3 , measurements at several positions along the wave tank), b) horizontal velocity profile at crest in breaking waves, c) wave length $\lambda/h_2 = (1/u_{max}) \int_{-\infty}^{\infty} u \, dx / h_2$ vs. u_{max}/c obtained in experiments (symbols) and in theory (solid and dashed lines). From Grue et al.¹⁶. Reproduced with permission by J. Fluid Mech.

depth outside ridge $h_1 = 45$ cm, upper layer depth $h_2 = 10$ cm, incoming (nondimensional) wave amplitude $a/h_2 = 0.59$, width of ridge 6.2 m, height of ridge above tank floor 30.5 cm, constant ridge slope ± 0.1 and top of ridge positioned 7.83 m from the endwall of the wave tank where the wave was generated. (There is a smooth transition at the top of the ridge between the two slopes.) The length of wave tank was 21.5 m.

The top of the ridge was in all experiments below the pycnocline at rest, and the upper layer was always thinner than the lower layer. The incoming waves were solitary waves of depression. During a strong interaction between wave and ridge the excursion of the pycnocline typically became lower than the mid depth of the water column. A significant distortion of the wave was observed as it encountered the turning point, i.e. the horizontal position (on the slope) where the pycnocline is half-way between the bottom and top of the water column. The incident depression wave was then transformed into a shorter leading depression and a subsequent dispersive wave train, where the first of the waves typically has a relatively high elevation. This process is the same as the one that occurs to a solitary wave of depression travelling up a sloping beach, beyond the turning point, described theoretically in Djordjevic and Redekopp⁴³, Knickerbocker and Newell⁴⁴, Malomed and Shrira⁴⁵ and experimentally by Helfrich, Melville and Miles⁴⁶. The process on the ridge develops a breaking of the wave in the form of mixing between salt and fresh water at the pycnocline, in the rear of the leading depression, and in the leading part of the subsequent wave of elevation. The mixing is visible as a fog in the upper picture in Fig. 10. A second breaking event occurs when the tail of the wave collapses due to the local strong steepness there, see the lower picture in Fig. 10. Estimates indicate a magnitude of the accelerations of about $0.5g'$ during the collapse. This means that a Rayleigh-Taylor instability is not the cause of the breaking.

Dispersion has a weak or strong effect on the incoming wave, depending on the slope of the ridge. If the slope is relatively small, dispersion has a stronger effect than indicated in Fig. 10, on the incoming depression solitary wave, as it arrives at the turning point. The wave is in the small slope case transformed into a relatively short leading depression that is decreasing in time, and a subsequent dispersive wave train, with a number of waves that gains in time. The dispersive wave train represents the origin of boluses - or vortex blobs - travelling up the slope, see the forthcoming section 6.2. If the ridge slope is relatively steep, and the waves have sufficiently large amplitude, wave breaking in the form of overturning is observed at the obstacle.

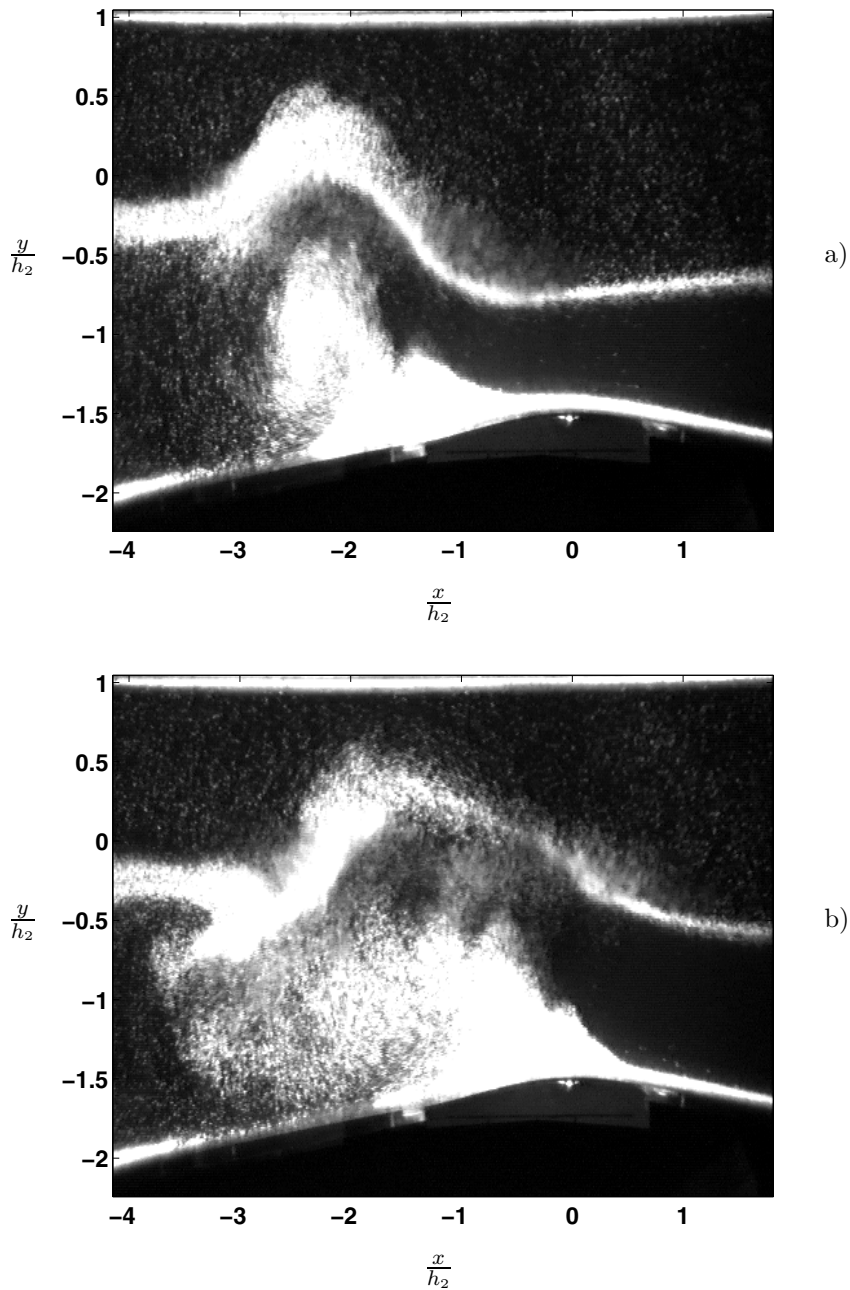


Fig. 10. Waves breaking at a ridge. Time difference 2.04 seconds. From Sveen et al.³¹. Reproduced with permission by J. Fluid Mech.

For a closer examination of the local process at the top of the ridge, prior to wave breaking, vertically averaged horizontal velocities in the upper and lower layer, \tilde{u}_2 and \tilde{u}_1 , respectively, are measured. Local thicknesses of the layers at the top of the ridge are defined by $\tilde{h}_{1,2}$ where the sum $\tilde{h}_1 + \tilde{h}_2$ equals the total depth of the fluid at the top of the ridge, see Fig. 11a. The values of \tilde{h}_1 and \tilde{h}_2 are obtained using $\tilde{u}_1\tilde{h}_1 + \tilde{u}_2\tilde{h}_2 = 0$, given $\tilde{h}_1 + \tilde{h}_2$. The local thicknesses of the layers define the local nonlinear shallow-water speed at the top of the ridge, serving as a reference speed, i.e. $\tilde{c}_0 = [g'\tilde{h}_1\tilde{h}_2/(\tilde{h}_1 + \tilde{h}_2)]^{1/2}$, where $g' = g\Delta\rho/\rho$, and the maximal value of \tilde{h}_2 and the minimal value of \tilde{h}_1 are used. The measured \tilde{u}_2 above the ridge show good correspondence with the fluid velocity in the upper layer due to the undisturbed incoming wave (results not shown). On the other hand, due to the thin local depth of the lower layer below the wave crest, at the top of the ridge, the magnitude of the velocity \tilde{u}_1 in the lower layer may become large. This is readily seen from the equation of continuity, i.e., $\tilde{u}_1\tilde{h}_1 + \tilde{u}_2\tilde{h}_2 = 0$, which means that if \tilde{h}_1/\tilde{h}_2 becomes small, $|\tilde{u}_1/\tilde{u}_2|$ becomes correspondingly large. This is characteristic for waves with large negative excursions. An example is displayed in Fig. 11b.

Measurements of $\tilde{u}_{1,2}/\tilde{c}_0$ show that breaking of incoming solitary waves of depression always occur when $|\tilde{u}_1|/\tilde{c}_0$ exceeds the value of 0.7, i.e. somewhat less than critical flows (Fig. 11c). This is a result from a total of 56 runs where the parameters in the experiments were: wave amplitude in the range 0.2–1.9 times the depth of the upper layer, ratio between the lower and upper layer depth in the range 3–8.5, and ridge slope in the range 0.1–0.33. Incipient wave breaking happens either in the form of local spilling or violent overturning of the waves. Shear instability, which plays no role in the initial part of the wave breaking process, is observed during the later stages in some of the breaking events. In all cases of breaking, vortices are shed on the up-slope side of the ridge. The (almost critical) lower layer flow at the slope is attached close to the top of the ridge, but separates at some point, as indicated in the photos in Fig. 10. The initial separation point is on the up-slope side. As a result of the separation, tracer particles are distributed vertically across the lower layer.

The transmitted waves exhibit a leading solitary wave with a subsequent dispersive wave train. The amplitude of the transmitted solitary wave corresponds in general to that of the incoming wave if breaking does not occur at the ridge. In the case of wave breaking the solitary wave undergoes a significant reduction in amplitude, however. The breaking process leads locally to a mixing between fresh and salt water at the ridge. Portions of mixed fluid that locally widens the pycnocline may subsequently generate

solitary waves of mode two propagating along the pycnocline, see Fig. 12. The induced velocity within the pycnocline, due to the mode two wave, is as large as 30 % of the horizontal fluid velocity due to the leading solitary wave of mode one, with nondimensional amplitude $a/h_2 = 0.35$ in the actual example. Generation of waves of mode two at a ridge has also been studied by Vlasenko and Hutter³⁰.

A corresponding interaction between an incoming solitary wave and a ridge is true also if the undisturbed upper layer has a linear stratification and the lower layer is homogeneous. A strong interaction between wave and ridge exhibits a pronounced increase of the lower layer velocity at the top of the ridge, a separation of the flow on the upwave side of the ridge and subsequent breaking of the wave. The reduction of the solitary wave amplitude due to the wave-ridge encounter is somewhat less pronounced if the upper layer is linearly stratified as compared to when the fluid is homogeneous (Guo et al.³²).

6. Wave breaking and run-up at a shelf-slope

6.1. Steep slope. Strong local breaking and mixing

Internal solitary waves that interact with a relatively steep shelf-slope (continuing through the entire water column) represented one of the focuses in the work by Kao et al.²⁰. They ascribed the breaking of the waves at the shelf, observed in their experiments, to shear instability. Michallet and Ivey²⁸ studied solitary waves of large amplitude that broke as they encountered the shelf-slope. In the latter work PIV was used to quantify the velocity fields. The mixing efficiency at the shelf and the magnitude of a reflected solitary wave travelling away from the beach were measured for wave slopes in the range 0.07–0.2. Michallet and Ivey suggested that the mechanism leading to breaking of the waves at the shelf was due to gravitational instability (this is not supported by our measurements), following the separation of the flow in the lower layer. The mixing efficiency was estimated from the difference between the initial density profiles and the density profiles at the shelf-slope after breaking. The main part of the mixing was found to occur in the lower layer. Their and our results for solitary depression waves interacting with a submerged ridge, presented in the previous section, are conform on this point.

The reflected to incident wave energy ratio (E_R/E_0) as function of the wave length to slope length ratio (L_W/L_S) was quantified. The results showed that $E_R/E_0 \simeq L_W/L_S$ for $L_W/L_S < 0.6$ and that a maximum value of $E_R/E_0 \simeq 0.65$ was reached for larger ratios of L_W/L_S . A strong

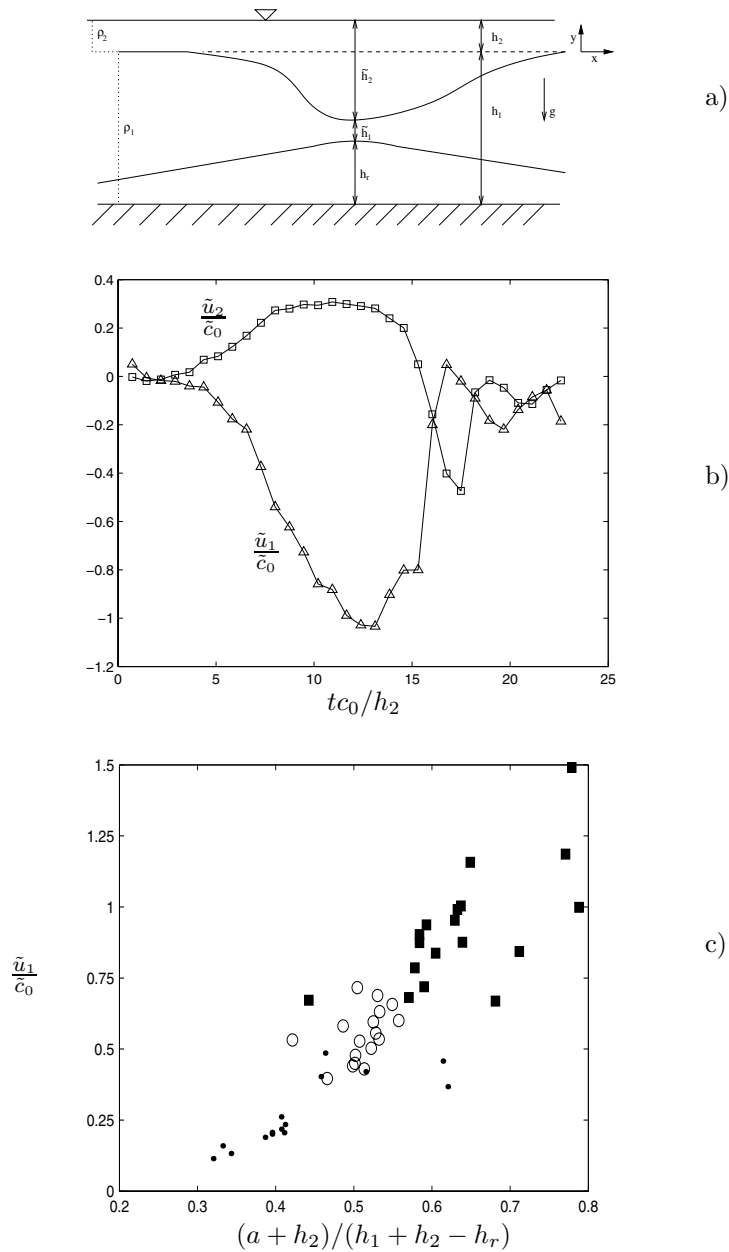


Fig. 11. Waves breaking at a ridge. a) Sketch, b) horizontal velocities at top of the ridge, c) in plot: breaking (filled squares), strong local deformation (open circles), weak interaction (dots). From Sveen et al.³¹. Reproduced with permission by J. Fluid Mech.

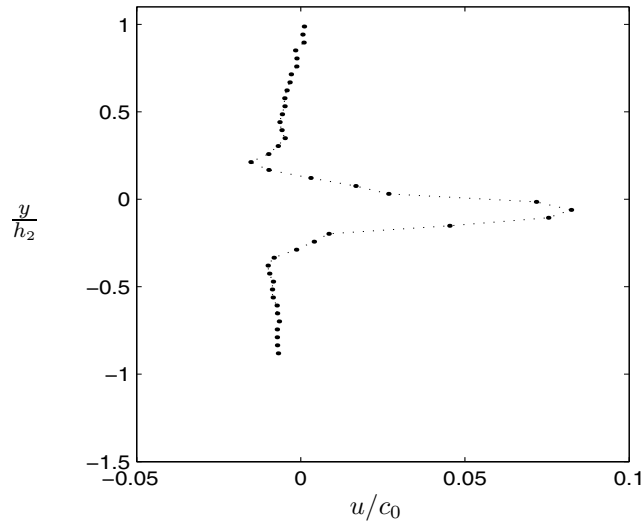


Fig. 12. Velocity profile in wave of mode two propagating along the pycnocline. From Sveen et al.³¹. Reproduced with permission by J. Fluid Mech.

flow up the slope in the form of a bolus could emerge from the interaction between the incident wave and the slope. After breaking, an off shelf flow was observed in the lower layer. Suspended particles were transported along the pycnocline. Particles that initially were located in the breaking region (at the slope) were spread far offshore.

6.2. Run-up at a shelf-slope

Relatively short incoming periodic waves or solitary waves of depression interacting with a weakly sloping beach show a transformation into boluses propagating up-slope (Cacchione and Southard²⁵, Wallace and Wilkinson²⁶, Helfrich²⁷). A solitary wave of depression may split into a shorter leading depression with a subsequent dispersive wave system, each individual wave developing into a bolus. This results in a sequence of boluses propagating up the slope (Fig. 15).

We shall here extend previous work, reporting experiments where the initial elevation or depression of the interface is very long. Our particular focus is strong run-up and strong currents that are generated where the pycnocline intersects the slope. The experiments are motivated by strong current events that have been observed at the sea floor at the offshore gas

field Ormen Lange. This is located in water 850 m deep on the slope of the Norwegian shelf. A thermocline at an average depth of about 500 m represents a characteristic feature of the ocean at the location. The thermocline separates the warm northward Norwegian Atlantic Current with temperature about $8\text{ }^{\circ}\text{C}$ from cold water masses in the deep ocean with temperature $-0.5\text{ }^{\circ}\text{C}$. Outside the shelf-slope, the lower cold layer has a thickness that is 1-2 times the depth of the upper warm water. (At the location of Ormen Lange the upper layer is thicker than the lower.) The relative density jump across the thermocline is 0.5×10^{-3} .

Fig. 13 shows a recording of a strong landward current event at the sea floor at the actual location. The recorded current speed has a maximum of 0.5 m/s (Fig. 13a). The flow direction is up the shelf-slope. There is only a very small velocity component along the shelf-slope. Prior to the current event the temperature at the sea floor exhibited a slow build-up phase reaching a maximum of $3\text{ }^{\circ}\text{C}$ (Fig. 13c). This indicates that the thermocline had moved downward the slope prior to the event, beyond the measurement position. The sudden return of the temperature coincides with the rapid increase of a current at the sea floor. The duration of the event is about 16–24 hours.

It is convenient to put the observed current on nondimensional form. As reference speed we use the linear long wave speed of the two-fluid system determined by $c_0 = [g'h_1h_2/(h_1 + h_2)]^{1/2} \sim 1.3\text{ m/s}$ where $g' = g\Delta\rho/\rho$ and we have put $h_2 = 500\text{ m}$ for the upper layer depth and the lower layer depth is determined by $h_1/h_2 = 2$. The maximum recorded speed of 0.5 m/s corresponds to about 40 % of the linear long wave speed. Further, the duration of the event corresponds to a nondimensional time tc_0/h_2 in the range 150–224. Observations of the thermocline motion in the ocean indicate that a strong current event may occur due to very long wave motion along the thermocline. Typical periods may be in the range 1-2 days. A corresponding estimated wave length is 100–200 km which means 200–400 times the upper layer thickness.

A set of model experiments in scale 1 : 5000 were undertaken in a small wave tank of length 7 m to shed light on the wave events observed at Ormen Lange (Sveen and Grue⁴⁷). The upper layer depth in the wave tank was $h_2 = 10\text{ cm}$, the lower layer depth in the deep water part $h_1 = 20\text{ cm}$ and the slope factor was $0.3\text{ m} / 7\text{ m}$ corresponding to 2.5 degrees. The lower layer of brine and upper layer of fresh water was separated by the pycnocline being about 1 cm thick. With a relative jump in density of 0.02 the linear long wave speed in the laboratory was 13 cm/s .

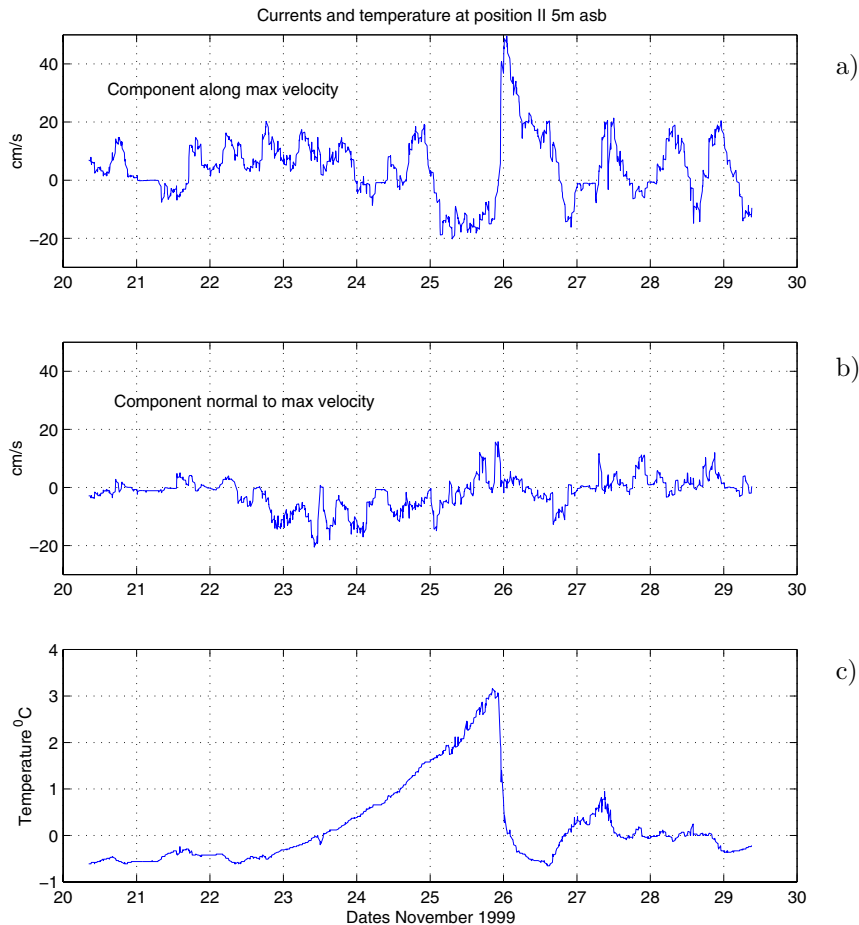


Fig. 13. Strong current event. Measurements 5 m above sea floor. Reproduced with permission by Norsk Hydro ASA.

Waves were generated by trapping a volume either of brine or fresh water behind the gate, elevating or depressing, respectively, the pycnocline relative to the level elsewhere in the tank (Fig. 14a). In the interest of investigating the response due to very long initial disturbances, the gate was placed 2 m from the end of the wave-generating part, corresponding to 20 times the upper layer thickness. Both an initial elevation and depression leads to the formation of a long bore at the point where the pycnocline intersects the shelf-slope. The bore propagates up the slope in the form of

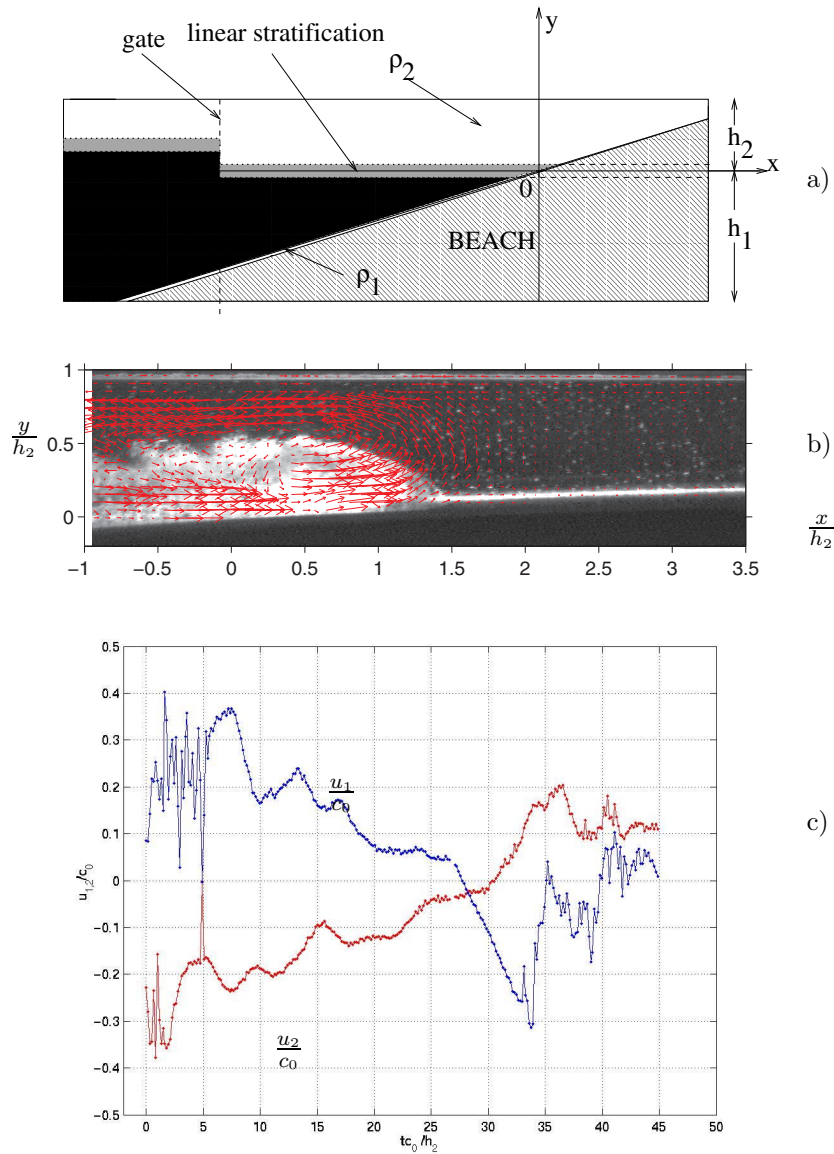


Fig. 14. Internal run-up on slope. a) Sketch of experiment, b) velocity field during internal wave run-up, c) induced horizontal velocities in lower (u_1) and upper (u_2) layer.

an internal run-up, with a leading part of the bore resembling the head of a gravity current (Simpson and Britter⁴¹, Simpson⁴²), see Fig. 14b. The induced fluid velocity in the head of the lower layer flow shows a maximal value of about 40 % of the linear long wave speed ($u/c_0 \simeq 0.4$), i.e. the same nondimensional speed as observed in the field (Fig. 14c). In the figure is plotted vertically averaged horizontal velocities in the layers.

The duration of the wave event in laboratory of $tc_0/h_2 = 40$ nondimensional periods is about 3 times shorter than in large scale. This difference is probably due to the relative difference of the input wave length in laboratory and large scale.

The most important point with the two-dimensional laboratory investigation was to estimate the magnitude of the fluid velocities that may be introduced during run-up of very long internal waves. The laboratory measurements may be used, e.g., as reference for simplified ocean model simulations in two dimensions with the rotation (of the earth) terms switched off. Three-dimensional and rotation effects should be included in full simulations of internal run-up.

7. Fish as markers of internal waves

In-situ registrations of internal wave motion were made by the Norwegian Institute of Marine Research in a small campaign off the Norwegian coast during August 1998. While the main objective was to register fish schools by means of echo-sounders, the data logs showed more than just the appearance of fish. A pronounced oscillatory motion of the schools became evident and were observed from both ship and buoy. The observations were made in the Norwegian Sea north of Sørøya in Finnmark at position 71°N $22^\circ 10'\text{E}$. A part of the record from the buoy is shown in Fig. 16 (Godø⁴⁸). It was evident that the fish was eating plankton that was drifting with the flow in the ocean. The motion of the individual fishes were traced by the data processing routines and are visible in the plot by small streaks. It can be concluded that the fishes serve as markers of an oscillatory vertical fluid motion in the sea, with an average level at 100 m depth, amplitude of 20 m at a depth of the sea of 146 m.

Hydrographical data from the area show that a roughly linear stratification in the upper part of the sea during late summer and autumn is developed annually. The thermocline is 200 m thick and has a relative density jump of 10^{-3} . The deep part of the sea has a constant density. Synthetic Aperture Radar (SAR) images from satellite were obtained during autumn 2000 and revealed occurrence of internal wave motion in the actual area in

the form of dispersive wave trains propagating from shallow to deep water. Wave lengths (from several images) were in the range 300–500 m.

We interpret the set of observations on basis of the experiments and theories of waves moving along the linearly stratified upper layer and the homogeneous lower fluid. Relevant for the actual observation we assume that the homogeneous lower layer is relatively thin compared to the thickness of the upper layer. The linear long wave speed is estimated using eq. (20) (see section 8.2 below) with $h_2 \gg h_1$, giving $c_0 \simeq N_0 h_2 / \pi \simeq 30$ cm/s. The Brunt-Väisälä frequency is determined by $N_0^2 = g \Delta \rho / (\rho h_2)$ with $h_2 = 146$ m. The equations (18)–(20) show that a wave length of $\lambda = 300$ m corresponds to a wave speed of 30 cm/s. The wave induced oscillatory vertical velocity at level 100 m becomes 12 cm/s at maximum, i.e. 40 % of the wave speed. The linear formulae predicts a horizontal surface velocity that somewhat exceeds the wave speed. The estimated wave period becomes 16 minutes (frequency 0.39 min^{-1}) which is significantly longer than indicated by the raw data from the echo-sounder (period 5 min, frequency 1.26 min^{-1}). (The buoy was drifting with the unmonitored surface current.) Recent measurements⁴⁹ in the area ($70^\circ 27,6'N$, $17^\circ 13,9'E$) reveal a maximal current speed of 65 cm/s, contributing to the frequency of encounter by an amount $Uk = 0.82 \text{ min}^{-1}$. This may explain the difference between the observed and estimated wave periods.

The wave trains are most truly tidally driven. The Atlas of the tides of the shelves of the Norwegian and Barents Seas (Gjevik, Nøst and Straume⁵⁰) exhibits dominating M_2 and S_2 modes with maximal currents at the location of about 25 cm/s and 10 cm/s, respectively. At spring tide the tidal current has a maximal speed of 35 cm/s. This corresponds to the magnitude of the linear long wave speed of the stratified fluid at the location. It is widely documented that a pronounced internal wave making may take place when the flow is close to critical, i.e. the bulk flow velocity is close to the linear long wave speed of the stratified fluid, see e.g., Grue et al.¹⁴.

8. Fully nonlinear reference models

For completeness we include a brief documentation of the fully nonlinear solitary wave models used in the reference computations.

8.1. Interface model

Several works on modelling fully nonlinear internal solitary waves are published (e.g. Amick and Turner¹⁰, Turner and Vanden-Broeck¹¹, Evans and

Ford¹³). Our method is based on the fully nonlinear transient interfacial model Grue et al.¹⁴, solving the Laplace equation in the layers, integrating the prognostic equations resulting from the kinematic and dynamic boundary conditions at the (moving) interface. The model accounts for full nonlinearity, full dispersion, any density or depth ratio, and puts no assumption on the wave length. The model was developed with the primary goal to compute transient waves. A version of the method to obtain waves of permanent form is derived (Grue et al.¹⁵, section 3.1). The coded method is fully documented and may be downloaded, see Rusås⁵¹. The main steps of the method which is used in the present computations are outlined. Solitary waves of permanent form are modelled in the frame of reference moving with the wave speed c . In this frame of reference the interface is “frozen”. There is a horizontal current in the far field with velocity $-c$. A coordinate system $O - xy$ is introduced with the x -axis at the level of the interface in the far field and the y -axis pointing upwards. We apply complex analysis and introduce the complex variable $z = x+iy$ and complex velocity $q_2(z) = \tilde{u}_2(x, y) - c - i\tilde{v}_2(x, y)$ in the upper layer and $q_1(z) = \tilde{u}_1(x, y) - c - i\tilde{v}_1(x, y)$ in the lower. The components $\tilde{u}_k - c$ and \tilde{v}_k ($k = 1, 2$) determine the horizontal and vertical components of the velocity field, respectively. At the top and bottom of the fluid layer the vertical velocity is zero. $q_1 + c$ and $q_2 + c$, being analytic functions, are found using Cauchy’s integral theorem, giving (the fluid in each layer is assumed incompressible, homogeneous and inviscid, and the motion irrotational)

$$PV \int_S \frac{q_2(z) + c}{z' - z} dz + \int_S \frac{q_2^*(z) + c}{z^* + 2ih_2 - z'} dz^* = \begin{cases} -2\pi i(q_2' + c), & z' \in \Omega_2 \\ -\pi i(q_2' + c), & z' \in S \end{cases} \quad (4)$$

in the upper layer, where $q_2' = q_2(z')$, and

$$PV \int_S \frac{q_1(z) + c}{z' - z} dz + \int_S \frac{q_1^*(z) + c}{z^* - 2ih_1 - z'} dz^* = \begin{cases} 2\pi i(q_1' + c), & z' \in \Omega_1 \\ \pi i(q_1' + V), & z' \in S \end{cases} \quad (5)$$

in the lower, where $q_1' = q_1(z')$. Here an asterix denotes complex conjugate, S the interface and Ω_k the domain of fluid number k . The interface S is parameterized by $z(\xi)$. (Scaled) tangential velocities are defined by $\Gamma_2 = q_2 dz/d\xi$ on the upside of the interface and $\Gamma_1 = q_1 dz/d\xi$ below. From (4) an integral equation to determine Γ_2 is derived:

$$\begin{aligned} -\pi(\Gamma_2 + Vx'_\xi) &= PV \int_I \operatorname{Re} \left(\frac{z'_\xi c y_\xi}{z' - z} \right) d\xi - \int_I \operatorname{Re} \left(\frac{z'_\xi c y_\xi}{z^* + 2ih_2 - z'} \right) d\xi \\ &+ \int_I \operatorname{Im} \left(\frac{z'_\xi}{z' - z} + \frac{z'_\xi}{z^* + 2ih_2 - z'} \right) (\Gamma_2 + cx_\xi) d\xi \end{aligned} \quad (6)$$

where $z_\xi = dz/d\xi$, $x_\xi = dx/d\xi$ etc. A similar equation is derived from (5) for determination of Γ_1 . The dynamic boundary condition at the interface gives:

$$\frac{1}{2|z_\xi|^2}(\rho_2\Gamma_1^2 - \rho_1\Gamma_2^2) - \frac{1}{2}(\rho_1 - \rho_2)c^2 + (\rho_1 - \rho_2)gy = 0 \quad \text{at} \quad S \quad (7)$$

where g denotes the acceleration of gravity. In the computations an equidistant distribution in x is applied. f_ξ and $f_{\xi\xi}$ are obtained by 5-point formulae. At the truncation of interface we impose: $y = y_\xi = y_{\xi\xi} = 0$. The equations are solved by an iterative scheme where in each step $\Gamma_1(x)$, $\Gamma_2(x)$, $y(x)$ and V are determined, given the amplitude or volume of the wave.

8.2. Fully nonlinear internal waves propagating along a linear upper stratification

Weakly or fully nonlinear models assuming a continuous and smooth density profile are developed in several works (Long⁵², Yih⁵³, Tung et al.⁵⁴; Turkington et al.⁵⁵, Brown and Christie⁵⁶). Here, the fully nonlinear integral equation method used in the computations included in section 4, is outlined. Waves of permanent form are modelled in the frame of reference moving with the waves (with a current with speed $-c$ at infinity). Assuming incompressible, inviscid fluid, and conservation of mass, gives, $\nabla \cdot \mathbf{v} = 0$, $\mathbf{v} \cdot \nabla \rho = 0$ where $\mathbf{v} = (u - c, v)$ denotes the fluid velocity. If a pseudo-velocity \mathbf{v}' is introduced by $\mathbf{v}' = (\rho/\rho_0)^{1/2}\mathbf{v}$, where ρ_0 is a reference density, and a pseudo-stream function Ψ' satisfies $\mathbf{v}' = \nabla\Psi' \times \mathbf{k}$ where $\mathbf{k} = \nabla x \times \nabla y$, it follows that $\rho = \rho(\Psi')$. The equation of motion gives

$$\rho_0 \nabla^2 \Psi' + gy \frac{d\rho}{d\Psi'} = \frac{dH(\Psi')}{d\Psi'}, \quad (8)$$

$$\frac{dH}{d\Psi'} = \left(\frac{dp}{dy} + \rho g \right) \frac{dy}{d\Psi'} + \frac{c^2}{2} \frac{d\rho}{d\Psi'} + gy \frac{d\rho}{d\Psi'}. \quad (9)$$

The vertical component of the equation of motion becomes in the far-field $p_y + \rho g = 0$, which means that the first term on the right of (9) is zero. The pseudo-stream function is then decomposed by $\Psi' = \Psi'_\infty + \psi'$, where Ψ'_∞ satisfies $d\Psi'_\infty/dy = -c(\rho/\rho_0)^{1/2}$, giving $\nabla^2 \Psi'_\infty = (c^2/2\rho_0)(d\rho/d\Psi')$. Since $d\rho/d\Psi'$ is constant along each streamline, (8) becomes

$$\rho_0 \nabla^2 \psi' + g(y - y_\infty) \frac{d\rho}{d\Psi'} = 0, \quad (10)$$

where y and y_∞ are vertical coordinates on the same streamline, with y_∞ in the far-field.

Applying the Boussinesq approximation ($\Delta\rho/\rho \ll 1$) we find $\Psi'_\infty = -cy[1 + O(\Delta\rho/\rho)]$, giving

$$y - y_\infty = \psi'/c. \quad (11)$$

Furthermore we have

$$\frac{g}{\rho_0} \frac{d\rho}{d\Psi'} = \frac{g}{\rho_0} \frac{d\rho}{dy} \frac{dy}{d\Psi'} \simeq \frac{N^2}{c} [1 + O(\Delta\rho/\rho)], \quad (12)$$

where $N^2 = -(g/\rho_0)(d\rho/dy)$ determines the Brunt-Väisälä frequency. Within the Boussinesq approximation we may replace the pseudo-stream functions (Ψ', ψ') by (Ψ, ψ) . The motion is thus governed by the Helmholtz equation, i.e. $\nabla^2\psi + \frac{N^2}{c^2}\psi = 0$.

A two-layer model where the undisturbed fluid has an upper layer with linear density profile and a lower layer with constant density is employed:

$$\rho(y) = \begin{cases} \rho_0 - \Delta\rho y/h_2, & \text{for } 0 < y < h_2, \\ \rho_0, & \text{for } -h_1 < y < 0. \end{cases} \quad (13)$$

The line $y = 0$ separates the two layers. At rest, the upper layer extends in the interval $0 < y < h_2$ and the lower layer in the interval $-h_1 < y < 0$. The Brunt-Väisälä frequency becomes constant in the upper layer, and is there determined by $N_0^2 = (\Delta\rho g)/(\rho_0 h_2)$. In the lower layer the Brunt-Väisälä frequency becomes zero. Let $\psi = \psi_2$ in the upper layer and $\psi = \psi_1$ in the lower. ψ_2 satisfies the Helmholtz equation in the upper layer, i.e. $\nabla^2\psi_2 + \frac{N_0^2}{c^2}\psi_2 = 0$. The stream function in the lower layer satisfies the Laplace equation, i.e. $\nabla^2\psi_1 = 0$. The upper boundary of the upper layer and the lower boundary of the lower layer are approximated by rigid lids. The two layers are separated by the streamline with vertical coordinate η where $\eta \rightarrow 0$ for $x \rightarrow \pm\infty$. The kinematic boundary condition requires that the fluid velocity is continuous at the boundary between the layers, i.e. that $\nabla(\psi_1 - cy) = \nabla(\psi_2 - cy)$ at $y = \eta$.

The stream functions are determined by

$$\psi_{1,2} = \int_I \sigma_{1,2}(s') G_{1,2}(x, y, x'(s'), y'(s')) ds', \quad (14)$$

where $\sigma_1(s)$ and $\sigma_2(s)$ are distributions, I the contour $y = \eta$ and s arclength along the streamline $y = \eta$. The Green function G_1 is a pole at $(x, y) = (x', y')$ and satisfies the Laplace equation, i.e. $G_1(x, y, x', y') = \ln(r/r_1)$. The other Green function is a pole at $(x, y) = (x', y')$ and satisfies the

Helmholtz equation, i.e. $G_2(x, y, x', y') = (\pi/2)[Y_0(Kr) - Y_0(Kr_2)]$, where Y_0 denotes the Bessel function of second kind of order zero and $K = N_0/c$. Furthermore, $r = [(x-x')^2 + (y-y')^2]^{1/2}$, $r_1 = [(x-x')^2 + (y+y'+2h_1)^2]^{1/2}$, $r_2 = [(x-x')^2 + (y+y'-2h_2)^2]^{1/2}$. The kinematic boundary condition at $y = \eta$ gives

$$PV \int_I \sigma_1(s') \frac{\partial G_1}{\partial s} ds' - c \frac{\partial \eta}{\partial s} = 0, \quad (15)$$

$$PV \int_I \sigma_2(s') \frac{\partial G_2}{\partial s} ds' - c \frac{\partial \eta}{\partial s} = 0, \quad (16)$$

$$-\pi[\sigma_1(s) + \pi\sigma_2(s)] + \int_I \left(\sigma_1(s') \frac{\partial G_1}{\partial n} - \sigma_2(s') \frac{\partial G_2}{\partial n} \right) ds' = 0, \quad (17)$$

where s denotes the arc length along the streamline $y = \eta$ and n the normal pointing out of the lower fluid layer.

The linear long wave solution of the mathematical problem is given by

$$\psi_2 = ac_0 \frac{\sin(N_0(y-h_2)/c_0)}{\sin(N_0h_2/c_0)} \cos \nu x, \quad (18)$$

$$\psi_1 = -ac_0(1 + y/h_1) \cos \nu x, \quad (19)$$

where ν denotes the wavenumber and c_0 the linear long wave speed. The latter is obtained by putting $\partial\psi_1/\partial y = \partial\psi_2/\partial y$ at $y = 0$, giving

$$\frac{N_0h_2}{c_0} \cot \frac{N_0h_2}{c_0} + \frac{h_2}{h_1} = 0, \quad (20)$$

where c_0 is obtained for N_0h_2/c_0 in the interval $(\pi/2, \pi)$.

9. Conclusion

Particle Tracking Velocimetry and Particle Image Velocimetry facilitate efficient and detailed recordings of velocity fields induced by internal wave motion. Global properties like wave speed and wave length are derived from the velocimetry. The laboratory measurements serve as references for fully nonlinear theoretical studies and confirm the applicability of the theories for a wide range of parameters. This is true for wave properties in a two-fluid system with constant density in the layers, for example. The experimental results, put on nondimensional form, may be used to predict internal wave

propagation and internal wave induced velocity fields in large scale. The wave tank experiments are used to explain observations of internal wave motion in the sea (Skagerak and the Norwegian Sea), indicating that the induced velocities may be rather strong. The laboratory experiments we refer to here were run with Reynolds number in the range $0.5 \times 10^4 - 3 \times 10^4$, where the Reynolds number is estimated from a typical velocity of the flow times a characteristic length scale, taken to be the thickness of the upper layer, divided by the kinematic viscosity of the water.

The laboratory simulations of internal wave motion are particularly useful beyond the range of validity of theoretical models. This is true for breaking flows induced by internal waves. Convective breaking of solitary waves propagating along a linear stratification in the upper part of the water column introduces a broadening of the waves, for example. This type of broadening differs from the one that takes place in a two-fluid system with constant density in the layers, where the waves are conjugate flow limited. The latter type of broadening is true for all depth ratios when the solitary waves are depression waves. Such a broadening is also true for solitary waves of elevation in the Boussinesq limit.

Solitary waves of depression may interact with a ridge that is located in the bottom of a two-fluid system with constant density in the layers. In such cases the PIV measurements show that breaking occurs when the induced fluid velocity in the lower layer, at the top of the ridge, exceeds 0.7 times the local (nonlinear) long wave speed. This conclusion is based on totally 56 experiments with wave amplitude in the range 0.2–1.9 times the upper layer depth, the ratio between the lower and upper layer depth in the range 3–8.5, and ridge slope in the range 0.1–0.33.

An important subject is interaction of thermoclines with a shelf-slope. Run-up of very long internal waves induces strong currents where the pycnocline intersects the slope. It is found that the maximal speed may be up to 40 % of the linear long wave speed of the two-fluid system. Such strong currents is a concern for industries operating in deep water. Breaking of the flow at the sloping bottom results in significant local mixing. It is observed that suspended fluid particles may be transported along the pycnocline, far off the shelf. Three-dimensional analysis of the motion of a stratified fluid at the shelf-slope represents a future challenge. An investigation combining precise laboratory experiments and theoretical ocean modelling may prove to be efficient. The effect of the earth rotation should be included in realistic predictions of internal run-up.

Breaking wave effects and the effect of shear instability represent important subjects where the use of PTV and PIV can still enhance our

knowledge. Experiments can be used to quantify the value of the Richardson number that corresponds to the onset of shear instability. For such experiments measurements of the density profile in the pycnocline (using e.g. Head probes or Schlieren technique) are required in addition to the velocimetry. Theories can be used to investigate the limit where u/c exceeds unity, indicating onset of convective breaking, and to compute the conjugate flow limit, indicating saturation of the wave amplitude and wave speed.

Vertical transport processes in the ocean represents another subject where more investigations are required. Supply of nutrient water masses from deep ocean to depleted water in shallow regions are important for the production taking place there, for example. We have in the experimental studies referred here, estimated the vertical transport of particles that may occur during breaking of the waves or in post breaking flows. We have found that the vertical transport is always very small, however. It may be true that vertical transport phenomenae occurring in the ocean cannot be properly modelled in the laboratory. One reason may be that the Reynolds number in the laboratory is relatively small. A more important reason may be that the time scale of the vertical processes taking part in the ocean is much longer than the time scale of the processes that can properly be modelled in laboratory scale.

Acknowledgments

This work was conducted under the Strategic University Programme ‘General Analysis of Realistic Ocean Waves’ funded by the Research Council of Norway. The data of the oscillatory fish motion provided by Dr. O. R. Godø, the assistance with the figures by J. K. Sveen and the technical assistance in the laboratory by A. Kvalheim and S. Vesterby are gratefully acknowledged.

References

1. A. R. Osborne, T. L. Burch and R. I. Scarlet, *J. Pet. Tech.* **30**, 1497 (1978).
2. L. A. Ostrovsky and Yu. A. Stepanyants, *Rev. Geophys.* **27**, 293 (1989).
3. J. M. Huthnance, *Geophys. Astrophys. Fluid Dyn.* **48**, 81 (1989).
4. R. D. Pingree and G. T. Mardell, *Prog. Oceanogr.* **14**, 431 (1985).
5. J. R. Apel, J. R. Holbrook, A. K. Liu and J. Tsai, *J. Phys. Oceanogr.* **15**, 1625 (1985).
6. T. P. Stanton and L. A. Ostrovsky, *Geophys. Rev. Lett.*, **25**, 2695 (1998).
7. B. Gjevik and S. E. Høst, *Naturen* **6**, 209 (1984).
8. J. Y. Holyer, *J. Fluid Mech.* **93**, 433 (1979).

9. D. I. Meiron and P. G. Saffman, P. G. *J. Fluid Mech.* **120**, 213 (1983).
10. C. J. Amick and R. E. L. Turner, *Trans. Am. Math. Soc.* **298**, 431 (1986).
11. R. E. L. Turner and J.-M. Vanden-Broeck, *Phys. Fluids* **29**, 372 (1986).
12. R. E. L. Turner and J.-M. Vanden-Broeck, *Phys. Fluids* **31**, 2486 (1988).
13. W. A. B. Evans and M. J. Ford, *Phys. Fluids* **8**, 2032 (1996).
14. J. Grue, A. Friis, E. Palm and P.-O. Rusås, *J. Fluid Mech.* **351**, 223 (1997).
15. J. Grue, A. Jensen, P.-O. Rusås and J. K. Sveen, *J. Fluid Mech.* **380**, 257 (1999).
16. J. Grue, A. Jensen, P.-O. Rusås and J. K. Sveen, *J. Fluid Mech.* **413**, 181 (2000).
17. G. K. Lamb, *J. Fluid Mech.* **451**, 109 (2002).
18. C. G. Koop and G. Butler, *J. Fluid Mech.* **112**, 225 (1981).
19. H. Segur and J. L. Hammack, *J. Fluid Mech.* **118**, 285 (1982).
20. T. W. Kao, F.-S. Pan and D. Renouard, *J. Fluid Mech.* **159**, 19 (1985).
21. H. Michallet and Barthélemy, *J. Fluid Mech.* **366**, 159 (1998).
22. R. E. Davis and A. Acrivos, *J. Fluid Mech.* **29**, 593 (1967).
23. T. Maxworthy, *J. Fluid Mech.* **96**, 47 (1980).
24. A. P. Stamp and M. Jacka, *J. Fluid Mech.* **305**, 347 (1995).
25. D. A. Cacchione and J. B. Southard, *J. Geophys. Res.* **79**, 2237 (1974).
26. B. C. Wallace and D. L. Wilkinson, D. L. *J. Fluid Mech.* **191**, 419 (1988).
27. K. R. Helfrich, *J. Fluid Mech.* **243**, 133 (1992).
28. H. Michallet and G. N. Ivey, *J. Geophys. Res.* **104**, 13467 (1999).
29. F. Wessels and K. Hutter, *J. Phys. Oceanogr.* **26**, 5 (1996).
30. V. I. Vlasenko and K. Hutter, *Nonl. Proc. Geophys.* **8**, 223 (2001).
31. J. K. Sveen, Y. Guo, P. A. Davies and J. Grue, *J. Fluid Mech.* **469**, 161 (2002).
32. Y. Guo, J. K. Sveen, P. A. Davies, J. Grue and P. Dong, *J. Environm. Fl. Mech.* (2004, to appear).
33. S. B. Dalziel, *Applied Scientific Research* **49**, 217 (1992).
34. C. E. Willert and M. Gharib, *Exp. in Fluids* **10**, 181 (1991).
35. J. Westerweel, D. Dabiri and M. Gharib, *Exp. in Fluids* **23**, 20 (1997).
36. J. K. Sveen, <<http://www.math.uio.no/~jks>> (1998).
37. L. A. Ostrovsky and J. Grue, *Phys. Fluids*, **15**, No. 10, 2934 (2003).
38. A. Carlin, Master thesis in Mechanics, Dept. of Math., Univ. of Oslo (2000).
39. K. Hald, Master thesis in Mechanics, Dept. of Math., Univ. of Oslo (2000).
40. D. M. Farmer and J. D. Smith, *Deep-Sea Res.* **27A**, 239 (1980).
41. J. E. Simpson and R. E. Britter, *J. Fluid Mech.* **94**, 477 (1979).
42. J. E. Simpson, *Ann. Rev. Fluid Mech.* **14**, 213 (1982).
43. V. D. Djordjevic and L. G. Redekopp, *J. Phys. Oceanogr.* **8**, 1016 (1978).
44. C. J. Knickerbocker, A. C. Newell, *Phys. Lett. A* **75**, 326 (1980).
45. D. Malomed and V. Shrira, *Physica D* **53**, 1 (1991).
46. K. R. Helfrich, W. K. Melville and J. Miles, *J. Fluid Mech.* **149**, 305 (1984).
47. J. K. Sveen and J. Grue, *This volume*, Chapter 9.5, (2004).
48. O. R. Godø, Personal communication, (2000).
49. V. Bakhanov, Personal communication, (2003).
50. B. Gjevik, E. Nøst and T. Straume, F&U report 90012, Statoil, Stavanger, Norway 74 pp. (1990).
51. P.-O. Rusås, <http://bukharin.hiof.no/~por/internalwaves/> (2000).

52. R. R. Long, *Q. J. R. Met. Soc.* **84**, 159 (1958).
53. C.-S. Yih, *J. Fluid Mech.* **9**, 161 (1960).
54. K. K. Tung, T. F. Chan and T. Kubota, *Stud. Appl. Math.* **16**, 1 (1982).
55. B. Turkington, A. Eydeland and S. Wang, *Stud. Appl. Math.* **85**, 93 (1991).
56. D. J. Brown and D. R. Christie, *Phys. Fluids* **10**, 2569 (1998).

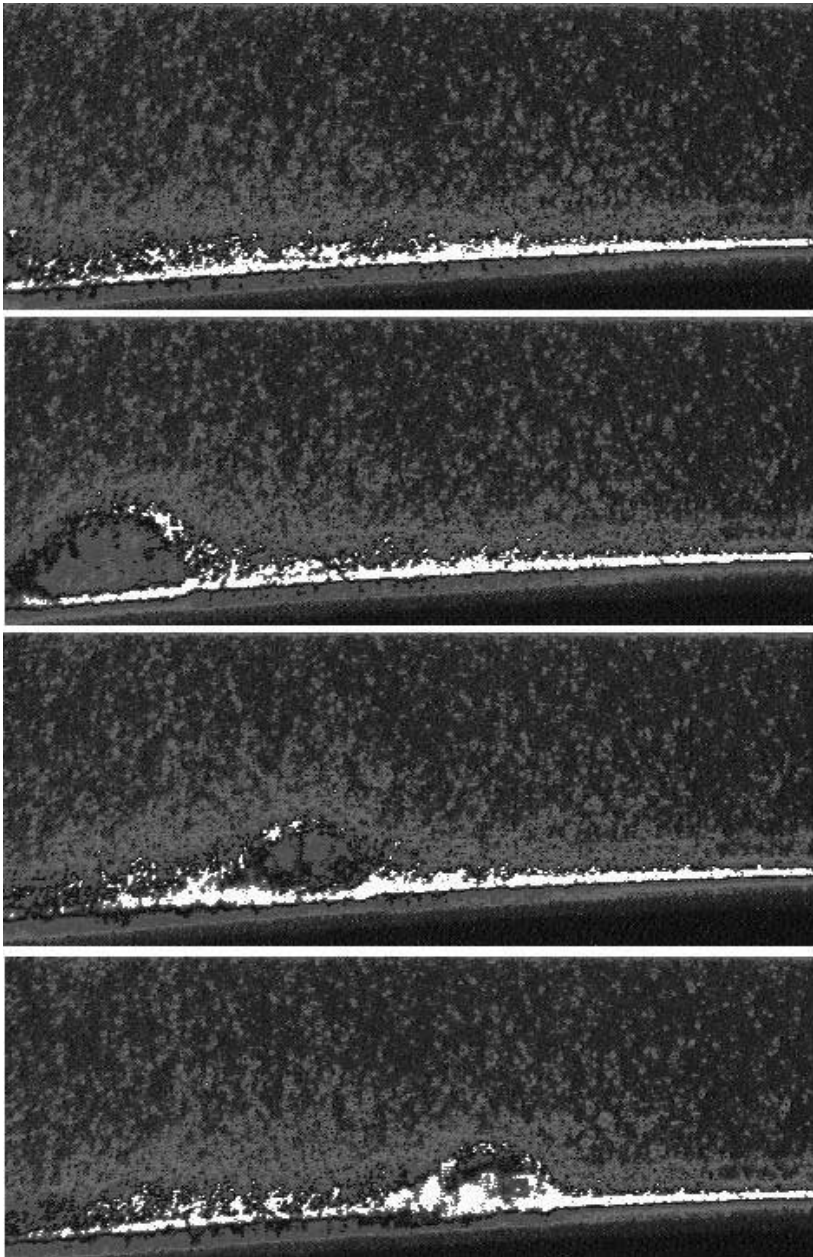


Fig. 15. Boluses running up slope. Free surface is at top of the figures.

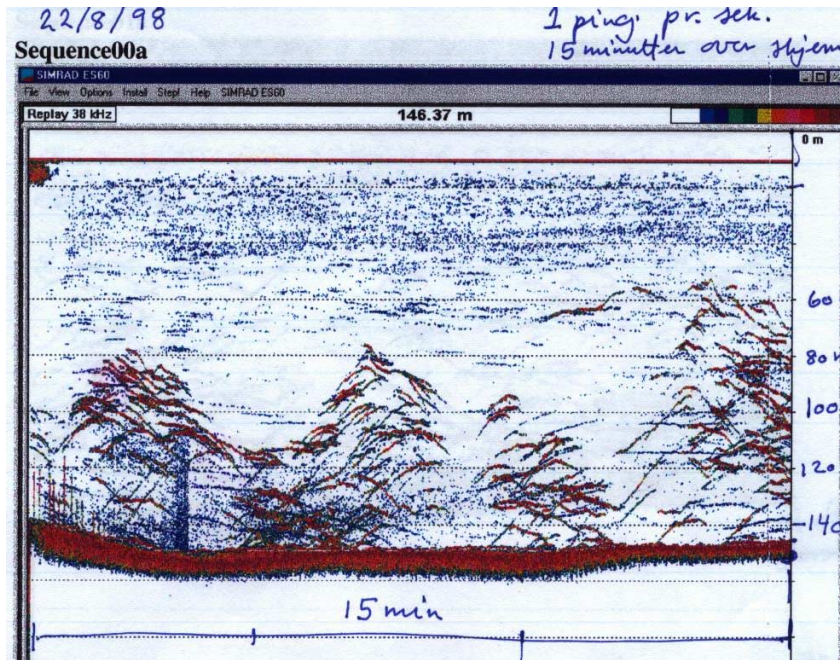


Fig. 16. Motion of fish school. Registrations by echo-sounders. Time variable along horizontal axis. Depth in meters are indicated. Total water depth at location: 146 m.